Spectral Energy Distributions and Optical Data Analysis of the TANAMI Sources

Presented by Miquela Stein

In partial fulfillment of the requirements for graduation with the Dean's Scholars Honors Degree in Astronomy.

Dr. Beverley Wills Supervising Professor	Date
Dr. Don Winget Co-Supervising Professor	Date
Dr. John Lacy Honors Advisor in Astronomy	Date

Spectral Energy Distributions and Optical Data Analysis of the TANAMI Sources

Department: Astronomy

Miquela Stein

Signature

Date

Dr. Beverley Wills

Signature

Date

Contents

Spectral Energy Distributions and Optical Data Analysis of the TANAMI Sources

Miquela Stein

May 1, 2015

Abstract

The TANAMI (Tracking Active Galactic Nuclei with Austral Milliarcsecond Interferometry) survey is a multi-wavelength study of 89 active galactic nuclei (AGN) seen in the southern hemisphere sky. This project uses archival data to display spectral energy distributions (SEDs) of each of the 89 sources, which are flux versus frequency plots of the sources over many regions of the electromagnetic spectrum from radio waves to gamma rays. Since blazars vary greatly over time, we propose an optical monitoring program for the MONET/South telescope in conjunction with ongoing monitoring projects in other wavelength bands.

1 Background and Introduction

1.1 Active Galactic Nuclei

1.1.1 Structure

Active galactic nuclei (AGN) are extremely high luminosity sources that emit radiation from around a supermassive black hole at the center of a galaxy. The material falling into the strong gravitational field near the black hole produces up to nearly 10^{14} $L_\odot$[21]. An AGN consists of a supermassive black hole (SMBH), surrounded by an accretion disk, a dusty torus, and narrow and broad line cloud regions, with relativistic jets perpendicular to the disk. The supermassive black hole mass is on the order of 10^8 $M_\odot$ up to 10^{10} $M_\odot$. The surrounding accretion disk has an inner region and an outer region. The inner region extends out to between 1.2 and 6 times the Schwarzschild radius, and the outer accretion disk continues to about 100 times larger in radius. Thus for a SMBH, the inner disk is around 10^9 to 10^{11} km in diameter, and the outer disk around 10^{11} to 10^{13} km in diameter.[2]. Above and below the accretion disk are clouds that have a broad emission line spectrum. These clouds are contained within a radius about ten times that of the accretion disk, on the order of 0.1 pc, or $3 \cdot 10^{12}$ km, for a 10^8 $M_\odot$ black hole. Perpendicular to the accretion disk are narrow relativistic jets of matter being expelled from the region surrounding the black hole. These narrow and highly variable jets can reach sizes of many kpc, and feed extended lobes, resulting from collisions with the dust and gas surrounding the galaxy, with the size of 100-1000 kpc. Surrounding the accretion disk is a large dusty torus, which can serve to obscure

the black hole when viewed directly onwards.The dusty torus is about 10 pc in size. Above and below the dusty torus are clouds which make up the narrow emission line region. The narrow emission line region is many parsecs to kpc in size, and is due to atomic lines produced by ionized hydrogen, oxygen, nitrogen, and other elements. The difference between narrow lines and broad lines is due to the velocity dispersion of the gas. Narrow lines are from a small velocity dispersion, and broad lines are from a large velocity dispersion.

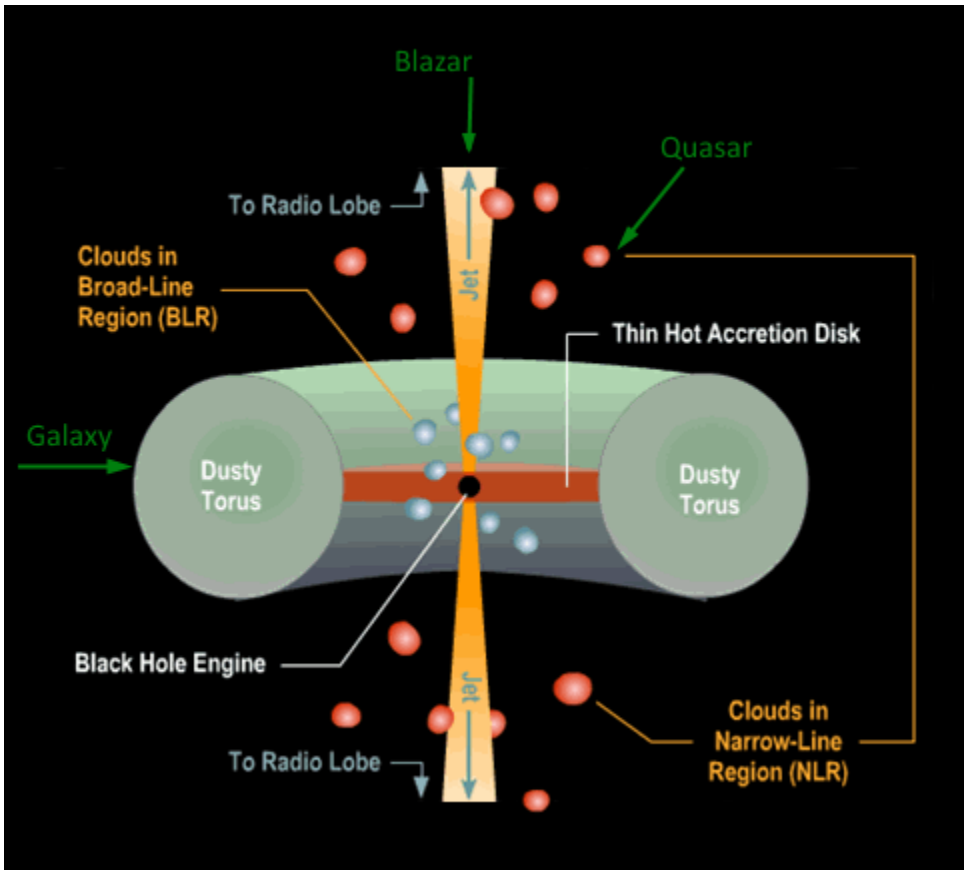

Diagram demonstrating AGN structure. (Credit: Brooks/Cole Thomson Learning)

1.1.2 Spectra and Classifications

In a simple view of AGN, we find there are three different types that we can observe, which are dependent on the angle that the AGN is with respect to the observer. If the AGN is oriented with the jet at a small angle to the observer, we refer to the AGN as a blazar. Blazars have a flat radio spectrum and extreme time variability, which is why we are interested in monitoring them. Most gamma ray sources are also found to be blazars. At larger angles with respect to the line of sight, we find that the accretion disk and broad line region usually dominate, which is a strong, broad-lined quasar. At even larger angles, if the observer is viewing the AGN directly or nearly in the direction through the dusty torus, then the inner AGN, accretion disk, and broad line region are obscured and mostly the torus and the lobes of the extended jets are visible, as well as the narrow line region. This type of source is referred to as a galaxy as by looking edge-on to the source it is possible to see the host galaxy of the AGN and light from

the nearby stars is prominent. It is possible to have cross-overs between the categories, as they also are defined by their spectra in addition to their viewing angle.

AGN radiate over a huge amount of the electromagnetic spectrum. The category of blazars can be subdivided based on their spectra. Within the TANAMI sample, we have the classifications of BL Lac, quasar, and galaxy. BL Lacs are blazars that have a flat radio spectra, and very weak or no broad emission lines in their optical spectra. Quasars have broad lines in their spectra. Galaxies mean that the source is close enough such that we can visibly resolve the AGN host galaxy or more frequently that the spectra is dominated by starlight from the surrounding galaxy.

Blazars exhibit Doppler boosting of their jets, and their spectra are often dominated by synchrotron radiation. This means that the spectra will peak in the infrared to ultraviolet and will show a flat radio spectrum. We find that AGN can be radio loud or radio quiet. Blazars have two types, those with broad emission lines, and those with weak or no broad emission lines. These differences are visible in their spectral energy distributions, from radio to gamma ray wavelengths. The broad lines are a result of the fast-moving gas with a velocity dispersion of $\sim$2000 to 10000 km/s.

When observing AGN, we see that the radio jets are extended, but the nucleus radiates as a point source. By viewing the full spectral energy distribution, we can learn more about what drives different parts of the emissions. Radio, x-ray, and gamma radiation comes from the jet, while infrared-ultraviolet radiation comes from the host galaxy, accretion disk, and ionized gas. We see absorption lines in this region, as the other regions have broad band emission and appear relatively featureless. By looking at the optical spectra emission lines, we can determine redshift, Doppler broadening effects, and other information useful for classifying a source.

1.2 Spectral Energy Distributions (SEDs)

We determine spectral energy distributions (SEDs) for all 89 of the TANAMI sources. To display the entire range of spectra, from radio to gamma ray, we use a spectral energy distribution (SED) plot. The SED is plotted on a log-log scale, with the log of the frequency, ν, in Hertz, versus the log of the frequency times the flux, νf_ν, in Jansky Hertz. This allows for the entire spectra to be displayed compactly on one graph. Blazars' SEDs show two peaks, a synchrotron peak in the infrared to UV region, and another, the result of inverse Compton scattered synchrotron radiation, peaking in the X-ray to gamma ray region. Synchrotron radiation comes from relativistic charged particles accelerating in a magnetic field and releasing electromagnetic radiation. Inverse Compton scattering is the result of relativistic particles scattering low energy photons to higher energies, so the two processes work together.

One of the aspects of the AGN that we can determine by looking at the SED is whether it is an HBL or an LBL source. HBL means that it is a High-frequency peaked BL Lac, and LBL means that it is a Low-frequency peaked BL Lac. This classification applies to all blazars, not just BL Lacs. Additionally, it has been found that many Flat Spectrum Radio Quasars (FSQR) have similar spectral features to LBLs.[4]

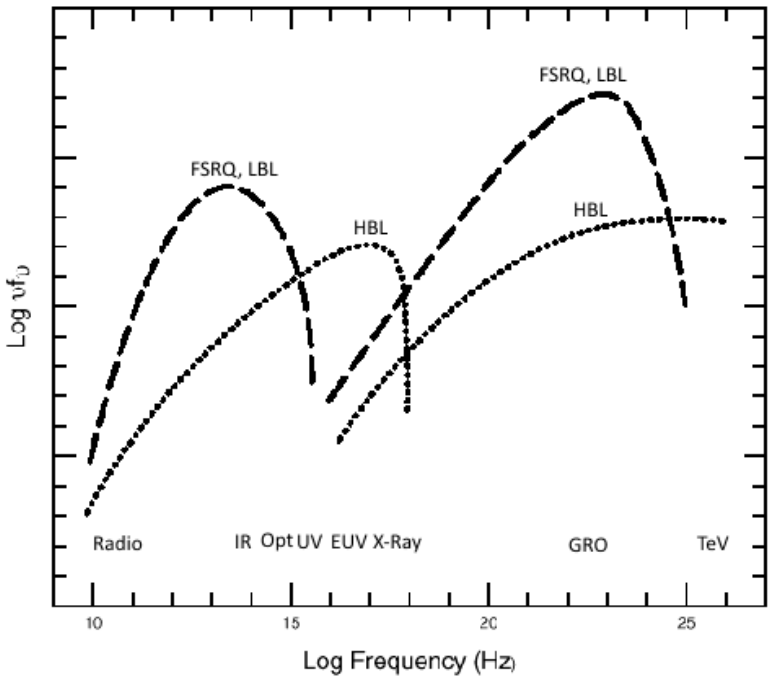

Figure demonstrating difference between HBL and LBL[4]

Below is an example of a spectral energy distribution from the TANAMI sample, with different frequency regions indicated.

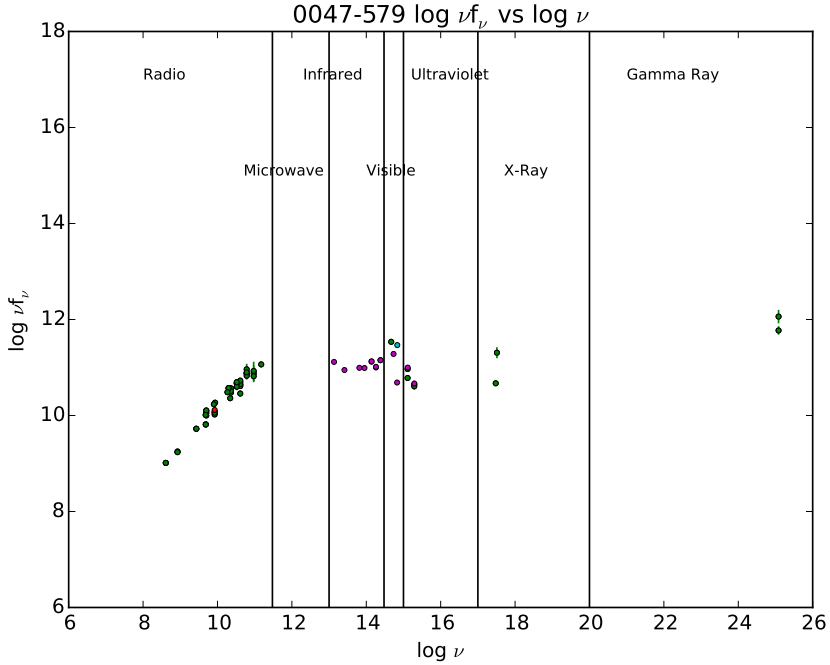

Spectral energy distribution of a source with frequency regions indicated.

1.3 TANAMI Background

The TANAMI (Tracking Active Galactic Nuclei with Austral Milliarcsecond Interferometry) survey collects data on southern hemisphere AGN with the Very Long Array (VLA) in Australia combined with multi-wavelength monitoring of the sources. Very Long Baseline Interferometry (VLBI) uses a series of radio telescopes spaced over a large fraction of Earth's radius to create images with very high angular resolution, on the order of milliarcsecond or less. The VLBI technique allows observers to map the structure of AGN jets that cannot be resolved with single-dish radio telescopes. Flat radio spectra usually indicates a blazar with high gamma ray activity. Nearly all gamma ray sources are blazars, with strong variable radio emission on the order of Janskys, and flat radio spectra.

The first set of TANAMI sources contained 43 southern sources south of $-30°$, with radio flux density $S_{5GHz} > 2$ Jy and a flat radio spectrum between 2.7 and 5 GHz. Additional sources have been added over time based on gamma ray observations from Fermi, bringing the sample to 75 sources. As more gamma ray sources have been detected and associated with radio-loud AGN, they have been added to the sample, bringing it to the current size of 89 sources.[1]

According to the TANAMI website, observations are made with the Australian/South-African Long Baseline Array (LBA+), using the antennas at Parkes, ATCA, Mopra, Hobart, Ceduna and the associated antennas Tidbinbilla, the IVS antennas TIGO, O'Higgins, and Hartebeesthoek. The group has also had occasional access to three 12m AuScope telescopes located near Hobart, Yarragadee and Katherine as well as a similar telescope in Warkworth, New Zealand. Observations at 8.4GHz and 22GHz are observed in typically 8 scans distributed over 12 hours, with target sources are monitored every $\approx$4 months. The TANAMI program is supported by an approved ATCA program for flux density monitoring between 6cm and 7mm, with largely overlapping target lists and a flux density monitoring program undertaken by the University of Tasmania, including the Ceduna and Hobart antennas. Simultaneous to TANAMI and Fermi observations, Swift UVOT/XRT observations are collecting UV to X-ray broadband source spectra.[10]

1.4 Project Justification

While quasi-simultaneous SEDs have been created for various individual sources, this project aims to use archival data to create an overall picture of the shapes of the SEDs, their time variability, and includes the data for all 89 sources. This paper will complement the ongoing TANAMI project containing radio through gamma ray data. By sorting the SEDs by class, we will be able to visualize differences between the SEDs for each of the classes. Additionally, we show that it is feasible to monitor more than half of the TANAMI sources in the optical region with the MONET/South telescope and propose an annual monitoring plan. Other telescopes monitoring the sources observe annually or semi-annually, and we plan to add MONET/South data to the quasi-simultaneous observations of these sources.

1.5 Introduction of Data Set

The current version of the TANAMI sample is shown below in Table 1. The 89 sources range in redshifts from z = 0.001825 to z = 2.47. All sources are below 30° South, and cover a roughly even distribution across the sky. We display two different classification types below. [1]Classification from TANAMI set from Dr. Matthias Kadler, has the types B: BL Lac object, G: Galaxy, Q: Quasar, and U: Unknown. [2]Spectral Classification of sources by Dr. Bev Wills, has the sources divided by spectral features. The codes are 1: Broad line region (BLR), even if it only has 1 broad line, 2: Very weak BLR, 3: Narrow emission lines (NEL), but no broad emission lines (BEL), 4: Host stellar absorption features visible, including diffuse interstellar bands (DIB), 5: Quasar (QSO) absorption limit, 6: Continuous spectrum, including continuous except for uncertain features (such as a BEL), 7: Photometric redshift. These codes are supposed to indicate the reliability of z (redshift), as well as spectrum class.[Private communication, Dr. Bev Wills, 2015] The redshifts indicated in the table reflect the most updated measurements available.

1.6 Database Information

NASA/IPAC Extragalactic Database (NED)[11], the Set of Identifications, Measurements and Bibliography for Astronomical Data (SIMBAD)[13], and VizieR[20] are databases of astronomical information that includes flux information and some spectral energy distributions of sources. The Veron 13$^{\text{th}}$ catalog contains optical information for some AGN.[16]

1.7 Optical Monitoring with MONET

The MOnitoring NEtwork of Telescopes (MONET) currently consists of MONET/North, located at the McDonald Observatory in Ft. Davis, TX, and MONET/South, located at the South African Astronomical Observatory in Sutherland, South Africa. The two telescopes are remotely operated and run by the University of Goettingen, Germany, and observe with visible and very near infrared filters. MONET/South is at the latitude of 30.3789° S, which allows it to observe a large range of the southern sky throughout the year, including the TANAMI sources. The primary mirror diameter is 1.20 m, and the camera it uses is SBIG STF-8300 M, and has the filters: Bessel U, B, V, R, and I, Sloan g', r', and z', H-α, OIII, and clear. The filters each accept photons of a narrow range of wavelengths, which correspond to the ultraviolet (U), blue (B), green or visible (V), red (R), and near infrared (I), and have central wavelengths from 360nm to 800nm.[7] These filters are useful because we can observe each of the sources with the U, B, V, R, and I, and get colors from the combination of these filters. We choose these five, since we already have data for them that is standardized to B, V, R. As the telescopes are remotely operated, the observer can collect data without having to be present at the telescope, and instead can be anywhere in the world. MONET/South is able to remotely observe the TANAMI sources, enabling semi-annual optical monitoring. This will go along with current monitoring by the VLA and surveys in the other wavelength bands. Monitoring of sources is important, as blazars are variable and tracking their evolution over time can provide us with insight to the internal structures and how they evolve.

Name (B1950)	NED Name	Class[1]	Class[2]	RA	Dec	Gal l	Gal b	Redshift
0047-579	[HB89] 0047-579	Q	1	12.49792	-57.64083	303.31305	-59.48635	1.792
0055-328	PKS 0055-328	B	?	14.5092929	-32.5724297	288.6104	-84.37119	>0.58
0208-512	[HB89] 0208-51	Q	6	32.6925	-51.01722	276.10173	-61.77812	0.999
0227-369	PKS 0227-369	Q	1	37.3685375	-36.7324503	243.93234	-67.17813	2.115
0235-618	PKS 0235-618	Q	1	39.2218571	-61.6042175	283.1959186	-51.2923425	0.465
0244-470	PKS 0244-470	Q	1	41.5	-46.855111	261.82839	-60.09404	1.385
0302-623	PKS 0302-623	Q	1	45.9609637	-62.1904303	280.22878	-48.68944	1.348
0308-611	PKS 0308-611	Q	1	47.4837467	-60.9775153	278.11751	-48.94118	1.479
0332-376	PMN J0334-3725	B	2	53.56425	-37.428806	240.15408	-54.38093	>0.39
0332-403	[HB89] 0332-403	B	2	53.55667	-40.14028	244.76383	-54.07512	1.351
0402-362	PKS 0402-362	Q	1	60.9739579	-36.0838644	237.74291	-48.48332	1.417
0405-385	[HB89] 0405-385	Q	?	61.7459804	-38.4411228	241.28697	-47.88986	1.285
0412-536	PMN J0413-5332	Q	1	63.32167	-53.53389	262.77422	-44.70337	1.024
0426-380	PKS 0426-380	B	5	67.1684342	-37.9387719	240.70795	-43.61817	1.11
0438-436	[HB89] 0438-436	Q	1	70.07167	-43.5525	248.41101	-41.56543	2.852
0447-439	PKS 0447-439	B	1	72.35292	-43.83583	248.80526	-39.91877	0.107
0454-463	[HB89] 0454-463	Q	1	73.96167	-46.26639	251.96828	-38.81424	0.8528
0506-612	[HB89] 0506-612	Q	1	76.68333	-61.16139	270.55042	-36.07211	1.089
0516-621	PKS 0516-621	B	2	79.1871925	-62.1181633	271.50966	-34.76123	1.300
0518-458	PICTOR A	G	1	79.95708	-45.77889	251.59678	-34.63435	0.035058
0521-365	ESO 362- G 021	B	1	80.74167	-36.45861	240.60775	-32.71592	0.055338
0524-485	PKS 0524-485	Q	1	81.5694633	-48.5102197	254.99272	-33.75513	1.299
0527-359	PMN J0529-3555	U	1	82.406958	-35.921222	240.31922	-31.28933	0.323
0530-485	PMN J0531-4827	U	?	82.994208	-48.459972	255.024737	-32.809741	–
0537-441	[HB89] 0537-441	B	1	84.70958	-44.08583	250.08276	-31.08983	0.894
0625-354	PKS 0625-35, OH-342	G	4	96.77792	-35.4875	243.45291	-19.96732	0.054594
0637-752	PKS 0637-752	Q	1	98.94375	-75.27139	286.36842	-27.15843	0.651
0646-306	PKS 0646-306	Q	1	102.058735	-30.73879	240.5384105	-14.1081876	1.153
0700-661	PKS 0700-661	B	6	105.1303	-66.179128	276.76852	-23.75943	>0.39
0736-770	PKS 0736-770	U	?	113.680615	-77.187158	289.13182	-24.05257	–
0745-330	PKS 0745-330	U	?	116.8320133	-33.1797144	248.42622	-3.99606	–
0823-500	PKS 0823-500	U	?	126.3619546	-50.1773575	266.648979	-7.0603194	–
0902-350	1FGL J0904.7-3514	U	?	136.176417	-35.239944	259.3696	7.8664	–
0920-397	[HB89] 0920-397	Q	1	140.69	-39.9930739	265.3516164	7.1903323	0.591
1036-529	PMN J1038-5311	U	?	159.669	-53.19525	283.721418	4.651828	–
1057-797	PKS 1057-79	B	1	164.6804571	-80.0650442	298.00945	-18.28811	0.581
1101-536	PKS 1101-536	U	6	165.96759	-53.9501933	287.4177	5.64963	> 0.24
1104-445	[HB89] 1104-445	Q	1	166.78625	-44.81889	284.17082	14.22016	1.598
1121-640	PMN J1123-6417	U	?	170.82833	-64.29694	293.55569	-3.04128	–
1144-379	[HB89] 1144-379	Q	1	176.75583	-38.20306	289.23978	22.95003	1.048
1257-326	PKS 1257-326	Q	1	195.1767746	-32.8866972	305.1776	29.94463	1.256
1258-321	ESO 443- G 024	G	4	195.25334	-32.441456	305.27388	30.38674	0.017042
1313-333	[HB89] 1313-333	Q	1	199.03333	-33.64972	308.80356	28.94032	1.21
1322-428	Cen A, NGC 5128	G	3,4	201.365	-43.01917	309.51584	19.41722	0.001825
1323-526	PMN J1326-5256	B	6	201.70292	-52.93944	308.3231	9.56163	>0.24

Name (B1950)	NED Name	Class[1]	Class[2]	RA	Dec	Gal l	Gal b	Redshift
1325-558	PMN J1329-5608	U	?	202.2547704	-56.1340739	308.18359	6.354	>0.13
1333-337	IC 4296	G	4	204.1625	-33.96583	313.53818	27.97306	0.012465
1343-601	Centaurus B	G	3	206.704346	-60.4081539	309.7214066	1.7315895	0.012916
1344-376	PMN J1347-3750	Q	1	206.9184537	-37.8435056	315.02538	23.70408	1.300
1424-418	[HB89] 1424-418	Q	1	216.98458	-42.10528	321.44739	17.2707	1.522
1440-389	PKS 1440-389	B	6	220.988321	-39.144369	325.64107	18.71501	>0.14
1451-375	[HB89] 1451-375	U	1	223.6142071	-37.79254	328.227438	18.9633163	0.314054
1454-354	PKS 1454-354	Q	1	224.36125	-35.65278	329.89401	20.53712	1.424
1505-496	PMN J1508-4953	U	?	227.16167	-49.88417	324.40048	7.18096	–
1510-324	PKS 1510-324	Q	?	228.4124583	-32.5831944	334.6775159	21.3802483	1.153
1549-790	PKS 1549-79	G	3	239.24542	-79.23444	311.17875	-19.4683	0.1501
1600-445	PMN J1604-4441	U	6	241.1292525	-44.692215	335.15576	5.76451	>0.01
1600-489	PMN J1603-4904	U	6	240.96167	-49.06833	332.15104	2.57308	–
1610-771	[HB89] 1610-771	Q	3	244.45542	-77.28833	313.43069	-18.8537	1.71
1613-586	PMN J1617-5848	U	1	244.32521	-58.80269	326.97026	-5.90314	1.422
1646-506	PMN J1650-5044	U	6	252.57076	-50.74815	336.13909	-3.9615	>0.09
1653-329	Swift J1656.3-3302	Q	1	254.0699	-33.036	350.599472	6.357102	2.4
1713-518	PMN J1717-5155	U	?	259.39667	-51.92222	337.77968	-8.07085	–
1714-336	PMN J1717-3342	B	?	259.4	-33.7025	352.73491	2.39222	–
1718-649	NGC 6328	G	3	260.92083	-65.01028	326.96822	-15.83243	0.014428
1733-565	PKS 1733-56	G	3	264.39917	-56.5675	335.37021	-13.01868	0.098
1759-396	PMN J1802-3940	Q	1	270.67792	-39.66889	352.45112	-8.4254	1.319
1814-637	PKS 1814-63	G	3,4	274.89583	-63.76333	330.85102	-20.76259	0.0627
1824-582	PKS 1824-582	U	1	277.30168	-58.23199	336.8284	-20.0165	1.520
1915-458	PKS 1915-458	Q	1	289.8195	-45.727389	284.935066	-23.310391	2.47
1933-400	PKS 1933-400	Q	1	294.3175	-39.96722	359.1626	-25.36603	0.970
1934-638	PKS 1934-63	G	3	294.8542754	-63.7126736	332.74613	-29.38934	0.18128
1954-388	[HB89] 1954-388	Q	1	299.49917	-38.75167	1.57899	-28.95812	0.626
2004-447	PKS 2004-447	G	1	301.9799346	-44.578965	355.3309216	-31.8498463	0.24
2005-489	[HB89] 2005-489	B	2,3,4	302.35583	-48.83167	350.37299	-32.60079	0.071
2027-308	PKS 2027-308	G	?	307.74125	-30.65667	12.62652	-33.68506	0.539
2052-474	[HB89] 2052-474	Q	1	314.06792	-47.24667	352.59044	-40.38119	1.489
2106-413	[HB89] 2106-413	Q	1	317.38833	-41.1725	0.67668	-42.83682	1.058
2123-463	PKS 2123-463	Q	7	321.6279342	-46.0966367	353.5862375	-45.6422272	1.46
2136-428	PMN J2139-4235	B	6	324.850667	-42.589	358.31741	-48.32616	>0.50
2142-758	PKS 2142-75	Q	1	326.8030429	-75.6036736	315.8042523	-36.5282324	1.139
2149-306	PKS 2149-306	Q	1	327.98125	-30.465	17.07691	-50.78449	2.345
2152-699	ESO 075- G 041	G	2	329.275	-69.69	321.31635	-40.64718	0.028273
2155-304	[HB89] 2155-304	B	4	329.71667	-30.22556	17.73049	-52.24562	0.116
2155-83	PKS 2155-83	Q	1	330.582208	-83.636528	307.961994	-31.746263	1.865
2204-540	[HB89] 2204-540	Q	1	331.93208	-53.77611	339.89751	-49.92575	1.206
2326-477	[HB89] 2326-477	Q	1	352.32375	-47.50528	335.72704	-64.05535	1.304169
2326-502	PKS 2326-502	Q	?	352.337	-49.9279667	331.9917208	-62.3135289	0.518
2355-534	[HB89] 2355-534	Q	1	359.47167	-53.18722	320.18535	-62.1104	1.006

Table 1: TANAMI Data Set

2 Methods

2.1 Spectral Energy Distributions

The spectral energy distributions were determined by collecting archival data from NED, SIMBAD, and VizieR. Additionally, in the thesis of Dr. Cornelia Mueller[1], new radio fluxes were added to the collection. By combining the data from NED with SIMBAD and the additional radio data, we find more complete spectral energy distributions for all of the sources. Each of the data points was converted to the standardized units of Jansky for measured flux, and Hertz for observational frequency. The log ν, frequency, versus the log νf_ν, the frequency multiplied by the flux, were plotted and software was written to automate the plotting. Thus a large collection of data points for each of the 89 sources was collected and the resulting SEDs are displayed in the appendix of this paper.

Within these databases, many observations made by Fermi, Swift, UVOT, and the 2MASS survey were used. According to NASA, the Swift telescope has three instruments which work together to provide rapid identification and multiwavelength follow-up of gamma-ray bursts (GRBs) and their afterglows. The wavelength ranges of these instruments are: Burst Alert Telescope (BAT): 15 – 150 keV, X-ray Telescope (XRT): 0.3 – 10 keV, and UV/Optical Telescope (UVOT): 170 – 600 nm. The Fermi Gamma-ray Space Telescope is a space mission that studies the sky in the energy range 10 keV – 300 GeV. The ranges measured for each instrument are: Large Area Telescope (LAT) 20 MeV – 300 GeV and Gamma-ray Burst Monitor (GBM) <10 keV – >25 MeV.[5],[9] The 2MASS (Two Micron All Sky Survey) survey, collected data in the near-infrared J (1.25 μm), H (1.65 μm), and K_s (2.16 μm) bandpasses for 99.998 percent of the sky.[15]

2.2 Optical Archival Data

By surveying the Veron 13$^{\text{th}}$ catalog, NED, and SIMBAD, we collected archival data for magnitudes of these sources in the optical and near-infrared bands of B, V, R, I, J, H, and K, as well as noting that some magnitudes are listed as O band, which is photographic plate data. We are also able to divide the data by the class of the source, which can be B, G, Q, or no class. Below is a table displaying the number of magnitudes found for each bandpass. For some bands, multiple magnitudes were listed for single sources and thus two magnitudes are included for some sources which results in the table reflecting higher counts for B, V, and R than the number of sources with data. By analyzing this data with Python, we are able to determine the characteristics of the sample in the optical regime, which helps us determine the plausibility of optical monitoring of this set.

Filter	B	V	R	I	J	H	K	O
Counts	78	67	84	4	41	45	42	14

2.3 Optical Monitoring Proposal

MONET uses timed block scheduling that operates with a merit function. The higher the merit, the more likely it is that an object will be observed. The merit function ranges from 10 percent to 90 percent, and has a defined starting date, duration, and transition time where merit level goes from its lowest to its highest values. For each of the sources in the TANAMI sample, we would choose to have the starting date and duration of potential observation centered around the optimal observation date.

By surveying the optical data from SIMBAD, we are also able to determine the sources that would be advantageous to monitor optically with the MONET/South telescope when it becomes operational again. Currently, according to the MONET website, MONET/South is unavailable for normal operations while the robotic software system and the new camera are being commissioned. We can determine the range of magnitudes of the already observed sources, and compare it to the magnitude cutoff for the MONET telescope in each of the filters.

2.3.1 MONET Exposure Time Calculator

The MONET telescope has an online calculator that allows the observer to determine the predicted signal to noise for a source with a certain magnitude and exposure time, with the specific camera on the telescope and observing conditions. The table of conditions are listed below. We have determined that a signal to noise ratio of 10 is the minimum value to discern the source, with a maximum allowed exposure time of 300 seconds. This exposure time is 5 minutes, which is around the longest exposure that can be safely taken without having to deal with the effects of the earth's rotation and imperfect tracking. With these two parameters, we determined a minimum brightness level for each of the filters, U, V, B, R, and I.[6]

MONET Exposure Time Calculator preset values:

Category	Parameter	Value	Units
Sky	Brightness (bright = 18-16)	22.0	magnitudes/sqr-arcsec
	Seeing	1.0	arcsecs
	Airmass	2.0	
	Extinction Coefficient	0.2	magn./airmass
Telescope: MONET	Aperture	1.2	m
	f/ratio	7	
	Total Reflectivity	0.73	
	Obscuration	0.1	
CCD Camera: SBIG ST-8300M (Current MONET/North camera)	Pixel Size	5.4	microns (unbinned)
	Binning	3	pixels
	Readout Noise	7.72	ADU
	Dark Current	0.02	ADU/pixel/s
	Gain	2.	e-/ADU
	Bias	1266	ADU/pixel
	Quantum Effiiciency	0.4	percent (at bandpass λ)
	Width	3326	pixels (unbinned)
	Height	2504	pixels (unbinned)
	Aperture Radius	2.0	seeing FWHM

The airmass used is 2.0, which corresponds to an elevation angle of 30°. The calculator has a bandpass section, below are the specifications for U, B, V, R, and I.

Bandpass	Parameter	Value	Units
U	Central Wavelength	365.00	nm
	Effective Width	54.00	nm
	Flux (magn = 0)	1810.00	Jy
B	Central Wavelength	440.00	nm
	Effective Width	97.00	nm
	Flux (magn = 0)	4260.00	Jy
V	Central Wavelength	550.00	nm
	Effective Width	88.00	nm
	Flux (magn = 0)	3640.00	Jy
R	Central Wavelength	700.00	nm
	Effective Width	161.00	nm
	Flux (magn = 0)	3080.00	Jy
I	Central Wavelength	900.00	nm
	Effective Width	171.00	nm
	Flux (magn = 0)	2550.00	Jy

The values able to be calculated are: Target Brightness (magnitudes), Exposure Time (seconds), and Signal-to-Noise. By choosing the values of exposure time and signal to noise (S/N), we are able to determine the faintest target brightness possible under the specifications for each filter. By varying the signal to noise for a certain exposure time and filter, we determine cutoffs for expected S/N levels for each of the filters.

2.3.2 Object Visibility Calculator and Observation Planner

The Staralt Object Visibility website is a resource for planning observations based on optimizing object visiblity each night. The website has several options for displaying the observability of objects. The *Staralt* setting plots altitudes of objects against time for a specific night. The *Startrack* plots the tracks of objects across the sky represented as a circle with the zenith at the centre. The *Starobs* plots the variation of altitude and observable hours of objects throughout a year. The *Starmult* prints a table with the best observing night for each object, its rising, culminating, and setting times, and moon parameters.[8]

The setting *Starmult* was used to determine optimal observation times throughout the year for each of the sources. This allows for planning of observations on with the MONET/South telescope on a yearly basis. The input used had the settings of: Mode: Starmult; Observatory Location: Sutherland Observatory (South Africa), 20.8117E - 32.3783N; Options: Minimum elevation: 10°, Maximum airmass: X = 5.8. Since the minimum elevation used in this calculator was 10°, and the MONET exposure time calculator used a minimum of 30°, we would expect that the sources are observable under the conditions predicted by the MONET calculator for shorter times than listed below. This does not otherwise affect the output below. The coordinates of each source were inputed, and the resulting output for each source had: Optimal observation date, Universal Time (UT) rise, UT culmination, Hours up, UT set, Moon distance, Moon

illumination. The optimal observation date is determined by maximizing the hours that the source is visible in a night. UT rise and UT set are the times that the source rises above or sets below the minimum elevation selected in UT time. UT culmination is the time at which the source reaches its highest point in the sky that night. Moon distance in degrees and percent moon illumination are given for middle-dark-time, which is defined as 12 hours after local apparent noon.

3 Results

3.1 Spectral Energy Distributions

Plots of the 89 sources are in the appendix, and we briefly discuss the overall aspects we find when sorting the sources by spectral classification in §4. The SEDs are displayed on a log ν – log νf_ν scale, with the frequency ranging from 10^6 to 10^{26} Hertz, which spans from radio to gamma ray. Each of the data points on the graph is an individual observation of the source at a defined frequency, with a resulting flux. The colors of the points on the graphs indicate their database source. Green points are from NED, blue points are from SIMBAD, purple points are from VizieR, and red points are from TANAMI/VLBI measurements at 8.4 GHz.[1] We also note that extinction coefficients have not been applied to the SED data.

3.2 Optical Archival Data Results

3.2.1 Individual Filters

Below are several graphs that statisically summarize the optical magnitudes. Additional graphs are supplied in the appendix. The below table shows the mean apparent magnitude of each band for all of the sources with error bars determined from a gaussian fit. The bands B, V, R, J, H, and K are the only bands with a significant number of sources and thus we disregard the I and O band results, but display them for completeness.

Band	Counts	Mean Mag.	St. Dev.
B	78	17.87	2.29
V	67	17.31	2.33
R	84	16.77	2.45
I	4	15.66	3.33
J	41	14.66	2.68
H	45	13.60	2.61
K	42	13.16	2.50
O	14	18.63	0.78

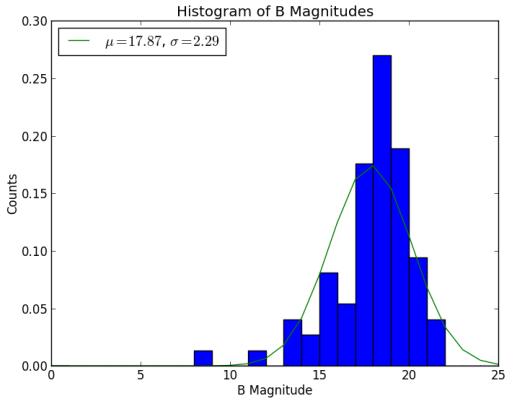
Histogram of B Magnitudes
$\mu = 17.87$, $\sigma = 2.29$
Counts
B Magnitude

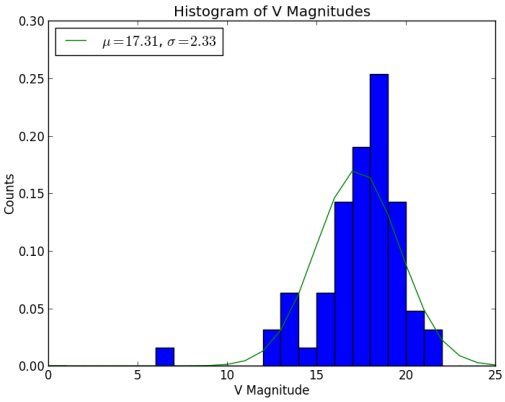
Histogram of V Magnitudes
$\mu = 17.31$, $\sigma = 2.33$
Counts
V Magnitude

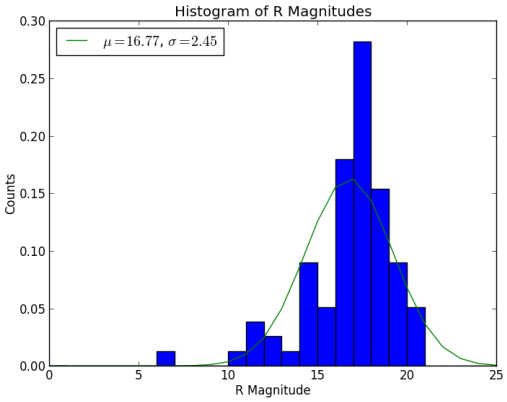
Histogram of R Magnitudes
$\mu = 16.77$, $\sigma = 2.45$
Counts
R Magnitude

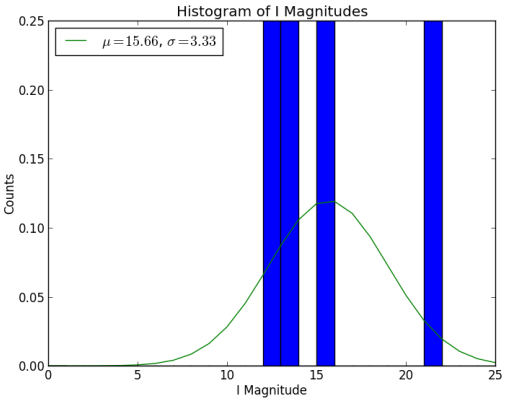
Histogram of I Magnitudes
$\mu = 15.66$, $\sigma = 3.33$
Counts
I Magnitude

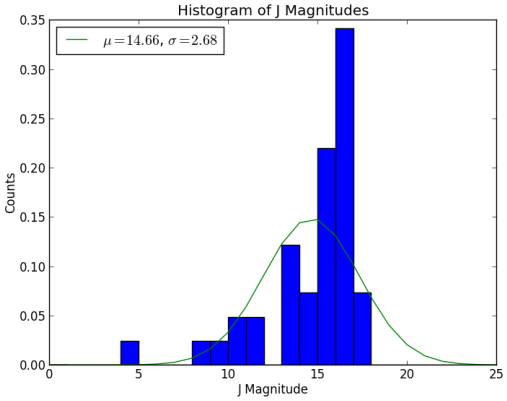
Histogram of J Magnitudes
$\mu = 14.66$, $\sigma = 2.68$
Counts
J Magnitude

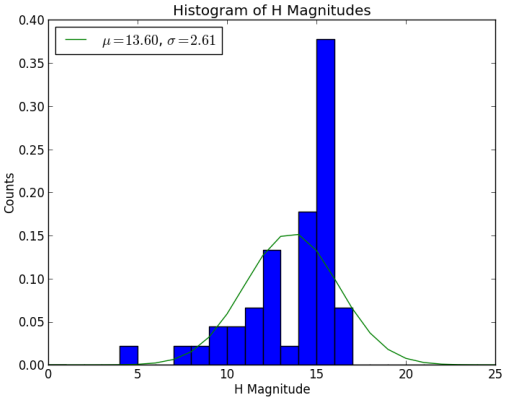
Histogram of H Magnitudes
$\mu = 13.60$, $\sigma = 2.61$
Counts
H Magnitude

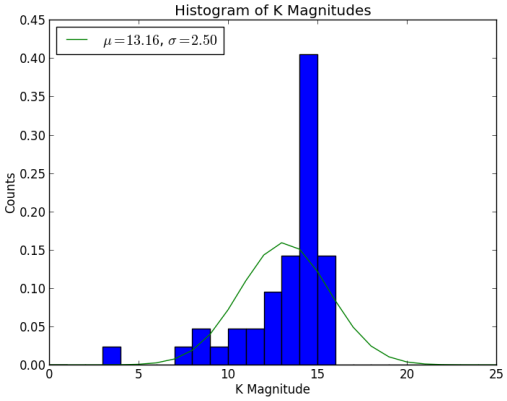
Histogram of K Magnitudes
$\mu = 13.16$, $\sigma = 2.50$
Counts
K Magnitude

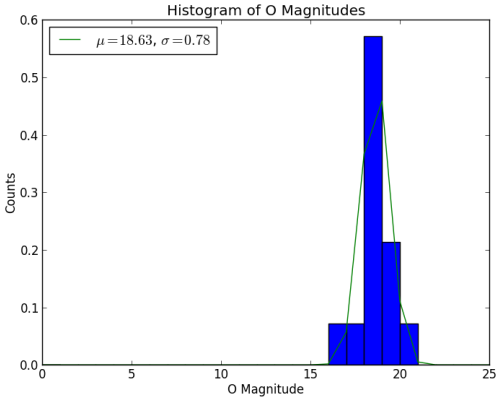
Histogram of O Magnitudes
$\mu = 18.63$, $\sigma = 0.78$
Counts
O Magnitude

Above, we see histograms the magnitudes in all 8 bands, along with a gaussian fit curve. This fit was chosen as a way of determining the mean magnitude as a reference for optical observation planning. The counts shown are normalized for the purpose of fitting the data. The appendix contains similar histograms of these sources, divided by class.

3.2.2 Color Index Reddening and Galactic Latitude

The color index is the difference in magnitudes between filters, with the longer wavelength filter magnitude being subtracted from the shorter wavelength filter magnitude, such as U–B, B–V, V–R, and R–I. This can be used to find the slope of a spectrum in a certain region, and provide information about the temperature of the source. To find a proper color index, the observations should be simultaneous. MONET observations would allow for an accurate measure of the colors of the sources, as we currently have values spanning a large range of time, and it is not valid to subtract these magnitudes from different observing runs to find the color of a source. By looking at the color, we can see how red the source is. Sources with a small color index are bluer and potentially hotter, and sources with a larger color index are redder and potentially cooler. Sources near the galactic plane, with galactic latitude close to zero, usually appear additionally reddened due to the extinction from the dust of the plane of the galaxy. This makes some sources appear fainter than they actually are and thus harder to observe in the optical.

The below graphs show the galactic latitudes of the 22 sources lacking at least two B, V, or R values, as well as the 8 sources lacking all three. This is useful because it shows us that they are clustered around the galactic plane, which suggests that we may end up with optical biases in our data due to the galactic plane blocking out these sources, or due to surveys not including the galactic plane. We plan to observe all 89 of the sources with MONET, and will account for galactic plane extinction in the data analysis. Some sources near the galactic plane will require an extinction correction.

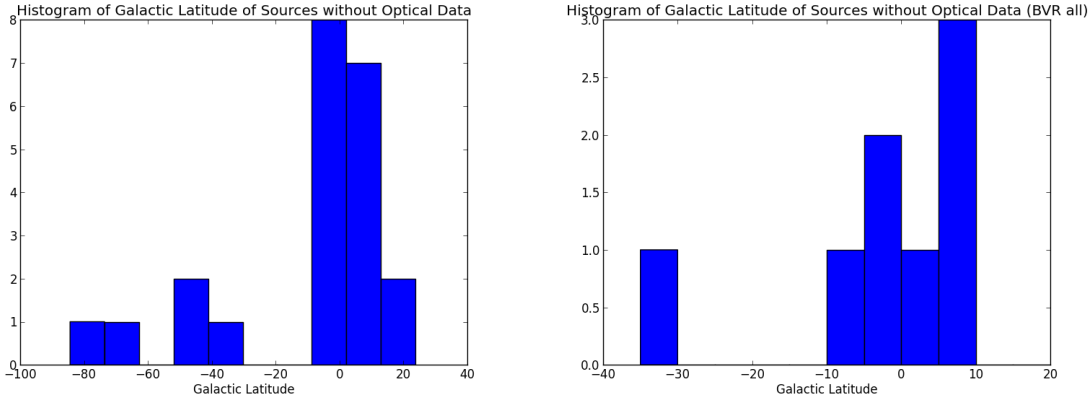

Left: Histogram of galactic latitude of sources lacking at least two B, V, or R values. Right: Histogram of galactic latitude of sources lacking all B, V, and R magnitudes.

3.3 Optical Monitoring Proposal

3.3.1 MONET Exposure Time Calculator Results

We have determined that a signal to noise ratio (S/N) of 10 is a minimum bound to identify a source, depending on brightness, and that a S/N ratio of 50 to 100 or above is reasonable to observe these sources. We have set the maximum exposure time to be 300 seconds (5 minutes), which is about the longest exposure that can be safely taken without having to deal with the effects of the earth's rotation and imperfect tracking mechanisms. With these two parameters, we determined a minimum brightness level for each of the filters, U, V, B, R, and I, by use of the exposure time calculator.

Below are the minimum magnitudes for various filters and S/N values with a constant exposure time of 300 seconds.

S/N	Filter	Mag.	Filter	Mag.	Filter	Mag.	Filter	Mag.	Filter	Mag.
10	U	20.71	B	21.97	V	21.50	R	21.69	I	21.32
50	U	18.93	B	20.19	V	19.72	R	19.92	I	19.54
100	U	18.13	B	19.40	V	18.93	R	19.12	I	18.74

Below are graphs of the minimum magnitude for each of the five filters to achieve a set S/N, as a function of exposure time.

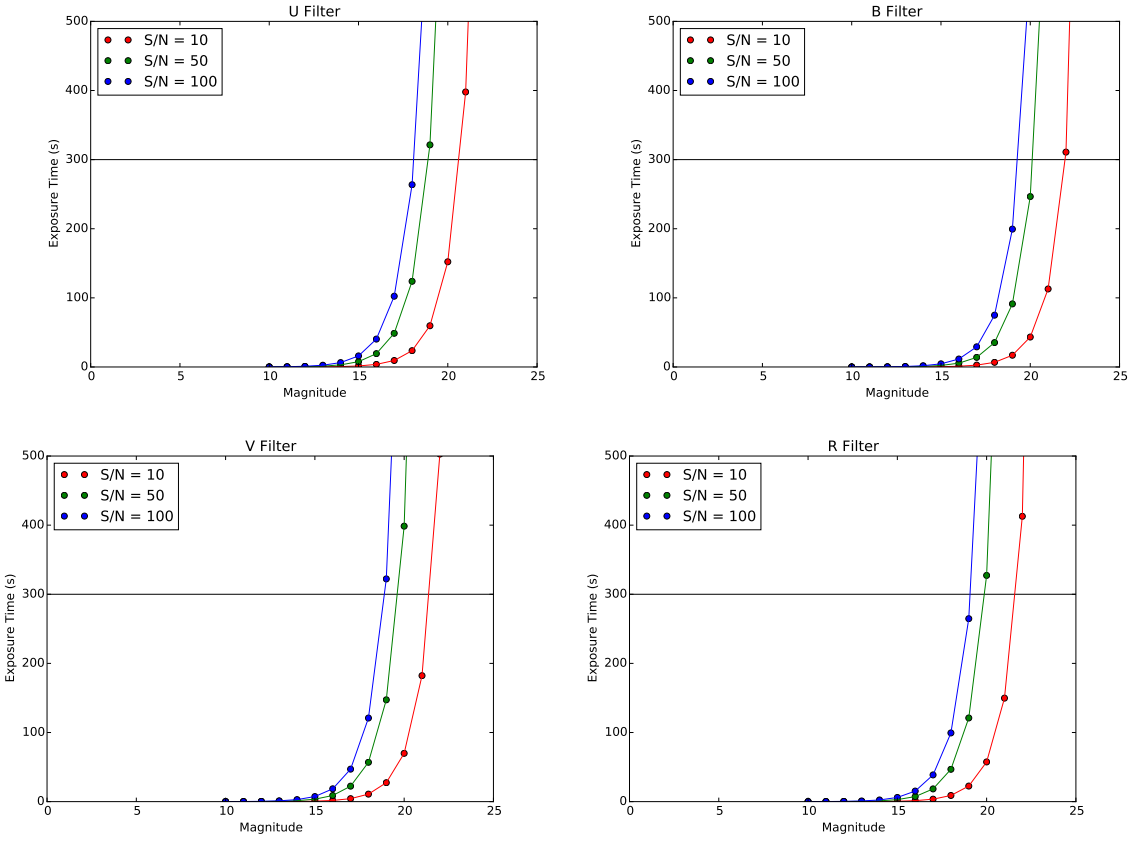

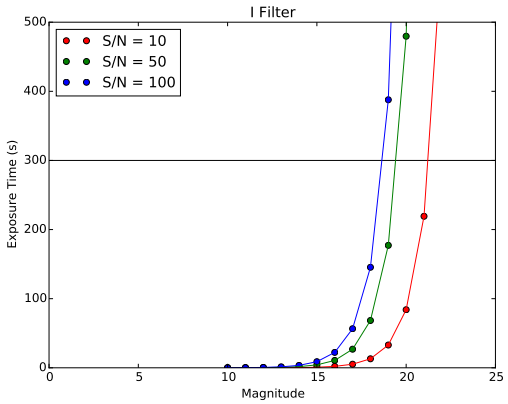

The reason these graphs peak very suddenly is due to the brightness of the source getting closer to the overall sky brightness. The MONET exposure time calculator has the sky brightness set at magnitude 22, which means that it becomes very difficult to observe sources at or near 22 magnitude in a reasonable amount of time.

The below graphs show these magnitude limits on the archival magnitude distributions for B, V, and R. The red line corresponds to a S/N of 10, the green line shows a S/N of 50, and the purple line shows S/N of 100.

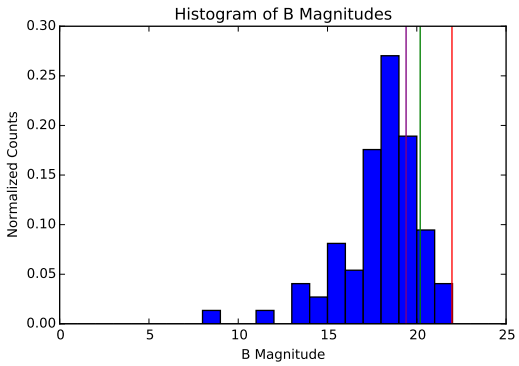

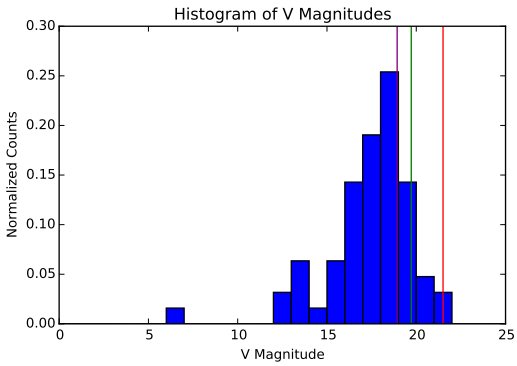

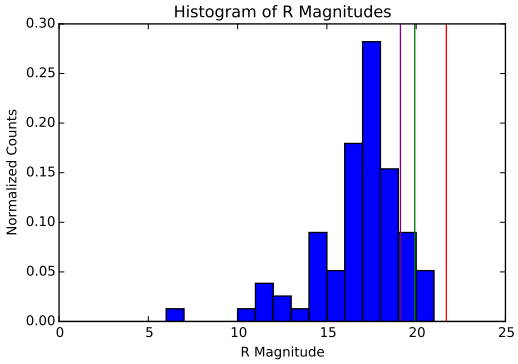

Of the 78 archival B magnitudes, we find that only 10 are between magnitudes of 20-22, and 3 that are between 21-22. Thus we would expect all sources to be observable with a S/N of at least 10, and around 87 percent to be observable at a S/N of at least 50. For the 67 V magnitudes, we find that 9 are between 19-20, 5 between 20-22, and 2 between 21-22. Therefore, almost all should be observable at a S/N of 10, 89 percent at 50 S/N or better, and about 79 percent with S/N at least 100. The 84 R magnitudes have 7 between 19-20 and 4 between 20-21. We see that all should be

observable with S/N 10, 95 percent with S/N 50 or better, and 87 percent with S/N 100 or better. Overall, we expect over 80 percent of all sources to be observable with a high S/N in all of the filters, which shows that optical monitoring of these sources with MONET/South is feasible and reasonable under the predicted conditions.

3.3.2 Optimal Observation Date Results

The TANAMI monitoring program started in 2007, and the VLBI observations are conducted two to three times per year.[17] Further radio observations with ATCA are taken more frequently.[18] The TANAMI group has a Swift fill-in program to get optical, UV and X-ray information. Additionally, since August 2008, the Fermi/LAT provides continuous gamma-ray monitoring for all sources. For some of the sources, there are also additional dedicated XMM, Suzaku, Chandra and HST observations in various wavelengths. With this information, we suggest monitoring all 89 sources at least one per year during their peak observing time. However, depending on simultaneity with other wavelength observations as well as telescope availability, it may be reasonable to observe these sources multiple times throughout the year.

Table 2 contains the results from the Starmult calculator. We find that for some of the sources, on the nights of optimal observation when they will be in the sky for the longest amount of time, there is a very large moon effect, and thus it may end up that these sources should be observed a week or two before or after their optimal observing date, especially if they are faint sources.

3.4 Introduction of MOJAVE and Comparison with TANAMI

The sample of MOJAVE 1.5Jy Flux Limited Sources has some similarities to the TANAMI sample. MOJAVE has a declination greater than $-30°$[19], and TANAMI has a declination less than $-30°$. If the selection criteria is similar enough, this makes a more complete sample of AGN across the entire sky. Both samples are divided with the same set of class types of BL Lac, Quasar, and Galaxy. Additionally both samples were chosen by observing bright sources in the radio wavelengths and determining a minimum brightness cutoff for a source to be added to the sample. However, the MOJAVE sample was chosen by $S_{2cm} > 1.5$ Jy, while the TANAMI sample was chosen with $S_{5GHz} > 2$ Jy. The radio wavelength of 2 cm corresponds to a frequency of 15 GHz, which shows that even though both samples were chosen with radio limits, they may not reflect the types of sources as the selection was defined for different wavelength regions. Additionally, the TANAMI sample includes the restriction of a flat radio spectra, and has additional sources added to the sample over time based on their gamma ray properties, unlike the MOJAVE sample. If one were to compare these samples in more depth, it would be necessary to note that although the samples have some similiarities, there are significant limitations to the comparison since the sources were chosen through different means. Below is a chart comparing the number of sources in each class for both samples.

Type	All Sources	BL Lac	Galaxy	Quasar	Unknown
TANAMI	89	16	14	41	18
MOJAVE 1.5Jy Flux Limited	183	29	8	143	3

Name	Date	UT Rise	UT Culm.	Hours Up	UT Set	M Dist.	M Ill.
HB89 0047-579	30-Sep	14h13m	22h45m	11h35m	7h17m	83	79
PKS 0055-328	2-Oct	16h 8m	22h45m	11h31m	5h22m	87	59
HB89 0208-512	19-Oct	15h 2m	22h51m	10h58m	6h39m	79	51
PKS 0227-369	23-Oct	16h 4m	22h54m	10h50m	5h44m	52	90
PKS 0235-618	25-Oct	16h 4m	22h54m	10h46m	5h44m	52	90
PKS 0244-470	27-Oct	15h26m	22h54m	10h43m	6h23m	62	96
PKS 0302-623	1-Nov	15h26m	22h54m	10h34m	6h23m	62	96
PKS 0308-611	2-Nov	15h26m	22h54m	10h32m	6h23m	62	96
PMN J0334-3725	9-Nov	15h59m	22h51m	10h20m	5h44m	128	0
HB89 0332-403	9-Nov	15h50m	22h51m	10h20m	5h53m	126	0
PKS 0402-362	16-Nov	16h 5m	22h53m	10h10m	5h41m	97	35
HB89 0405-385	17-Nov	15h57m	22h53m	10h 8m	5h48m	89	46
PMN J0413-5332	19-Nov	14h48m	22h51m	10h 5m	6h54m	77	68
PKS 0426-380	23-Nov	15h57m	22h51m	10h 0m	5h45m	54	98
HB89 0438-436	26-Nov	15h36m	22h50m	9h57m	6h 5m	65	94
PKS 0447-439	29-Nov	15h32m	22h48m	9h54m	6h 3m	79	72
HB89 0454-463	1-Dec	15h21m	22h46m	9h52m	6h12m	90	53
HB89 0506-612	4-Dec	15h21m	22h46m	9h49m	6h12m	90	53
PKS 0516-621	6-Dec	15h21m	22h46m	9h48m	6h12m	90	53
PICTOR A	7-Dec	15h23m	22h47m	9h47m	6h10m	113	6
ESO 362- G 021	8-Dec	15h57m	22h46m	9h47m	5h35m	123	2
PKS 0524-485	9-Dec	15h 9m	22h45m	9h46m	6h21m	113	0
PMN J0529-3555	10-Dec	15h57m	22h45m	9h45m	5h32m	125	0
PMN J0531-4827	11-Dec	15h 7m	22h43m	9h45m	6h19m	111	2
HB89 0537-441	13-Dec	15h25m	22h42m	9h44m	5h59m	109	13
PKS 0625-35, OH-342	27-Dec	15h49m	22h35m	9h44m	5h21m	63	86
PKS 0637-752	29-Dec	15h49m	22h35m	9h45m	5h21m	63	86
PKS 0646-306	2-Jan	16h 0m	22h32m	9h47m	5h 3m	51	98
PKS 0700-661	6-Jan	16h 0m	22h32m	9h50m	5h 3m	51	98
PKS 0736-770	15-Jan	16h 0m	22h32m	9h59m	5h 3m	51	98
PKS 0745-330	18-Jan	15h49m	22h28m	10h 3m	5h 7m	129	0
PKS 0823-500	29-Jan	14h38m	22h22m	10h18m	6h 7m	77	85
1FGL J0904.7-3514	8-Feb	15h37m	22h22m	10h35m	5h 7m	67	71
HB89 0920-397	13-Feb	15h19m	22h21m	10h45m	5h22m	104	22
PMN J1038-5311	3-Mar	14h24m	22h25m	11h19m	6h27m	60	99
PKS 1057-79	8-Mar	14h24m	22h25m	11h29m	6h27m	60	99
PKS 1101-536	9-Mar	14h21m	22h27m	11h32m	6h33m	61	77
HB89 1104-445	10-Mar	15h 7m	22h26m	11h34m	5h46m	65	68
PMN J1123-6417	14-Mar	15h 7m	22h26m	11h42m	5h46m	65	68
HB89 1144-379	20-Mar	15h32m	22h27m	11h54m	5h22m	142	3
PKS 1257-326	6-Apr	15h55m	22h33m	12h27m	5h11m	39	88
ESO 443- G 024	6-Apr	15h57m	22h34m	12h27m	5h10m	39	88
HB89 1313-333	10-Apr	15h53m	22h33m	12h35m	5h13m	81	52
Cen A, NGC 5128	12-Apr	15h22m	22h35m	12h39m	5h47m	100	30
PMN J1326-5256	12-Apr	14h36m	22h36m	12h39m	6h35m	95	30

Name	Date	UT Rise	UT Culm.	Hours Up	UT Set	M Dist.	M Ill.
PMN J1329-5608	13-Apr	14h14m	22h34m	12h40m	6h55m	103	20
IC 4296	14-Apr	15h57m	22h38m	12h42m	5h19m	128	11
Centaurus B	17-Apr	15h57m	22h38m	12h48m	5h19m	128	11
PMN J1347-3750	17-Apr	15h43m	22h37m	12h48m	5h31m	152	0
HB89 1424-418	27-Apr	15h29m	22h38m	13h 6m	5h47m	69	76
PKS 1440-389	1-May	15h40m	22h38m	13h12m	5h36m	32	98
HB89 1451-375	3-May	15h47m	22h41m	13h15m	5h34m	23	99
PKS 1454-354	4-May	15h53m	22h40m	13h17m	5h26m	26	96
PMN J1508-4953	7-May	14h56m	22h39m	13h22m	6h22m	57	76
PKS 1510-324	8-May	16h 3m	22h40m	13h11m	5h17m	66	66
PKS 1549-79	19-May	16h 3m	22h40m	13h38m	5h17m	66	66
PMN J1604-4441	21-May	15h21m	22h40m	13h40m	5h59m	121	24
PMN J1603-4904	21-May	15h 0m	22h39m	13h40m	6h18m	120	24
HB89 1610-771	24-May	15h 0m	22h39m	13h44m	6h18m	120	24
PMN J1617-5848	24-May	15h 0m	22h39m	13h44m	6h18m	120	24
PMN J1650-5044	2-Jun	14h51m	22h38m	13h52m	6h26m	34	97
Swift J1656.3-3302	4-Jun	15h58m	22h36m	13h16m	5h15m	42	87
PMN J1717-5155	9-Jun	14h44m	22h38m	13h56m	6h32m	102	35
PMN J1717-3342	9-Jun	15h58m	22h38m	13h20m	5h18m	105	35
NGC 6328	11-Jun	15h58m	22h38m	13h57m	5h18m	105	35
PKS 1733-56	14-Jun	14h14m	22h38m	13h58m	7h 2m	140	0
PMN J1802-3940	21-Jun	15h36m	22h36m	13h56m	5h36m	104	35
PKS 1814-63	26-Jun	15h36m	22h36m	13h57m	5h36m	104	35
PKS 1824-582	28-Jun	15h36m	22h36m	13h57m	5h36m	104	35
PKS 1915-458	12-Jul	15h 6m	22h30m	13h48m	5h53m	145	5
PKS 1933-400	16-Jul	15h31m	22h32m	13h42m	5h33m	145	3
PKS 1934-63	17-Jul	15h31m	22h32m	13h43m	5h33m	145	3
HB89 1954-388	22-Jul	15h32m	22h29m	13h31m	5h26m	86	47
PKS 2004-447	24-Jul	15h12m	22h31m	13h35m	5h49m	66	66
HB89 2005-489	25-Jul	14h51m	22h28m	13h34m	6h 6m	56	76
PKS 2027-308	30-Jul	15h59m	22h30m	13h 2m	5h 2m	19	99
HB89 2052-474	5-Aug	15h 2m	22h32m	13h18m	6h 2m	96	51
HB89 2106-413	9-Aug	15h24m	22h29m	13h12m	5h35m	137	13
PKS 2123-463	13-Aug	15h 6m	22h31m	13h 5m	5h56m	143	0
PMN J2139-4235	16-Aug	15h21m	22h32m	13h 0m	5h42m	126	9
PKS 2142-75	18-Aug	15h21m	22h32m	12h57m	5h42m	126	9
PKS 2149-306	19-Aug	16h 2m	22h32m	12h51m	5h 3m	103	32
ESO 075- G 041	20-Aug	16h 2m	22h32m	12h53m	5h 3m	103	32
HB89 2155-304	20-Aug	16h 5m	22h35m	12h53m	5h 6m	93	41
PKS 2155-83	21-Aug	16h 5m	22h35m	12h51m	5h 6m	93	41
HB89 2204-540	23-Aug	14h28m	22h32m	12h48m	6h37m	60	71
HB89 2326-477	11-Sep	15h 8m	22h39m	12h12m	6h10m	136	0
PKS 2326-502	11-Sep	14h56m	22h39m	12h12m	6h22m	134	0
HB89 2355-534	18-Sep	14h39m	22h40m	11h58m	6h41m	88	35

Table 2: Starmult Calculator Results

4 Discussion

4.1 Spectral Energy Distribution Characteristics by Class

We find that for the SEDs on average there is much more data available in the synchrotron emission range than the inverse Compton scattering range. When we divide the sample by class, we can determine some interesting features that characterize each of the groups. For the galaxy class objects, we find that there are frequently much higher fluxes in the optical than the radio. This is likely due to the additional light from the stars of the host galaxy, which provides an additional boost to the spectra. Examples of this are the sources 1258-321, 1333-337, and 1718-649, which show a clear jump from the radio to the optical, even when variability is taken into account. Many of the BL Lac objects and quasars appear to have similar trends, however we find HBLs in the BL Lacs, whereas in the quasars we see almost entirely LBLs. Some examples of potential HBL BL Lac objects are 1440-389, 2005-489, and 2155-304. These sources appear to have the synchrotron peak in the ultraviolet or higher, as opposed to the infrared to optical region where the LBLs peak. Even though we are able to define some general characteristics, we find that within the entire sample, the specific location of the synchrotron peak varies greatly between sources. A useful observation is the relative strength of the radio to the optical, as many sources have data in both of those regions. By comparing the strength, it is possible to get a better idea of the location of the synchrotron peak for each of the sources. In many of the sources we find obvious signs of variability, such as the source 0537-441, which again reinforces the need for simultaneous measurements. Another cause of scatter may be due to a source being extended in a certain wavelength, such as an extended radio source or optical light from a host galaxy, which we have already demonstrated.

4.2 2027-308: Reclassification of a Source

While examining the data set, we found that a source was misclassified. Based on the radio coordinates associated with the source, it was determined that 2027-308 was not the bright nearby galaxy of ESO 462- G 027, with z = 0.019764, but instead is a source about an arcmin south of the bright ESO galaxy. The proper source is PKS 2027-308, with z= 0.539 as determined from the spectra. It is still believed to be classified as a galaxy, as it has narrow emission lines, no broad lines, and a flat radio spectrum.

5 Future Work

As there is now sufficient information to create a full monitoring proposal for TANAMI sources using MONET/South, we recommend implementing the monitoring program as soon as the telescope becomes operational. With MONET/South data, we would be interested in finding out the color indices for the sample and determining how the color relates to the classification. Additionally, expanding the monitoring to other wavelengths would greatly improve the data available for creating spectral energy distributions and would augment the current understanding of each of the sources.

6 Appendix

6.1 Optical Data

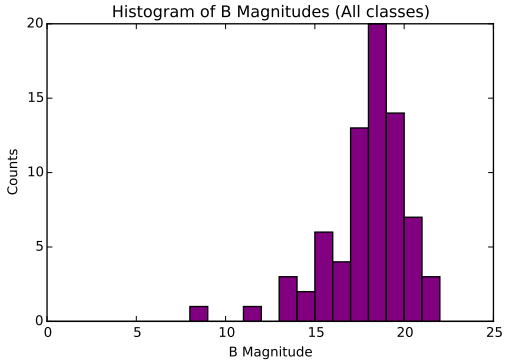

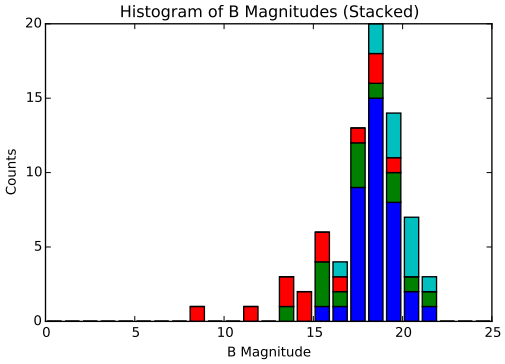

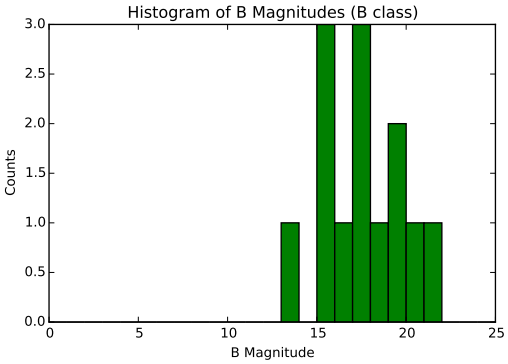

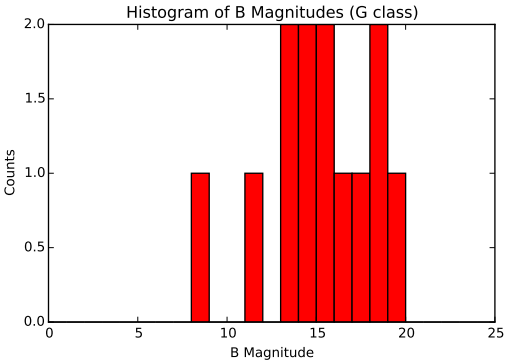

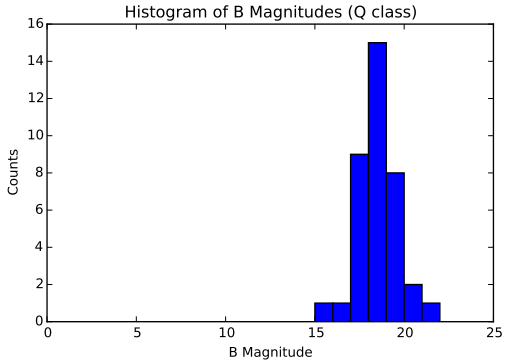

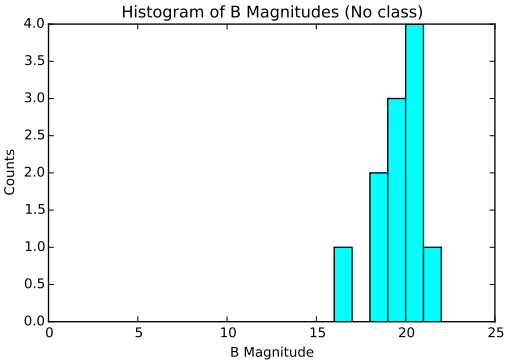

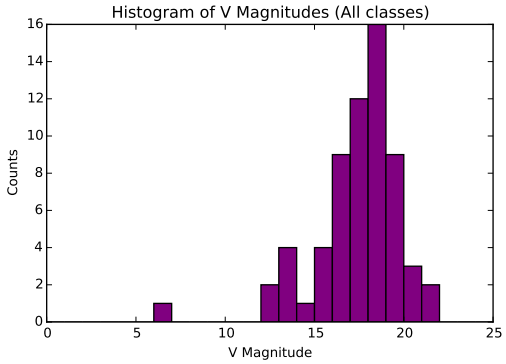
Histogram of V Magnitudes (All classes)
Counts
V Magnitude

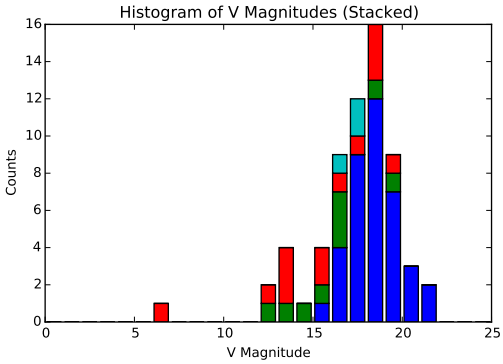
Histogram of V Magnitudes (Stacked)
Counts
V Magnitude

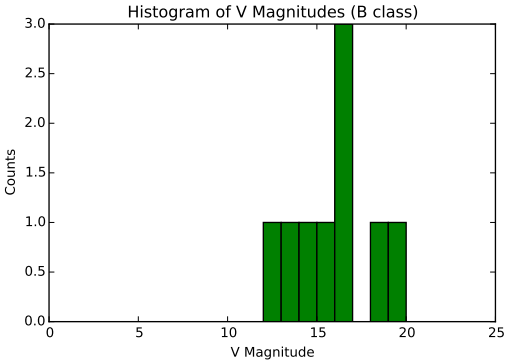
Histogram of V Magnitudes (B class)
Counts
V Magnitude

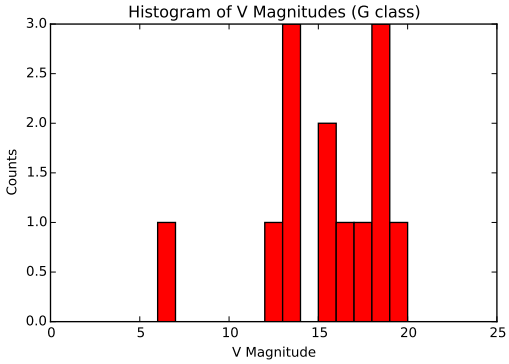
Histogram of V Magnitudes (G class)
Counts
V Magnitude

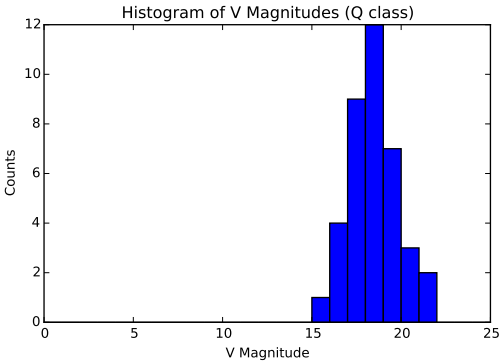
Histogram of V Magnitudes (Q class)
Counts
V Magnitude

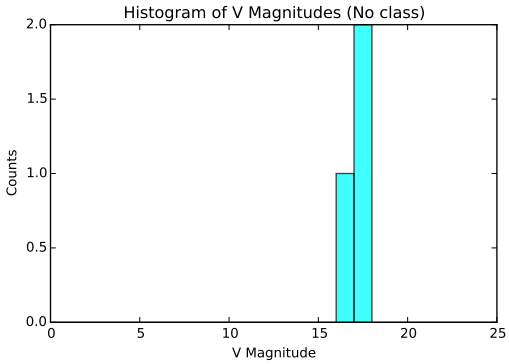
Histogram of V Magnitudes (No class)
Counts
V Magnitude

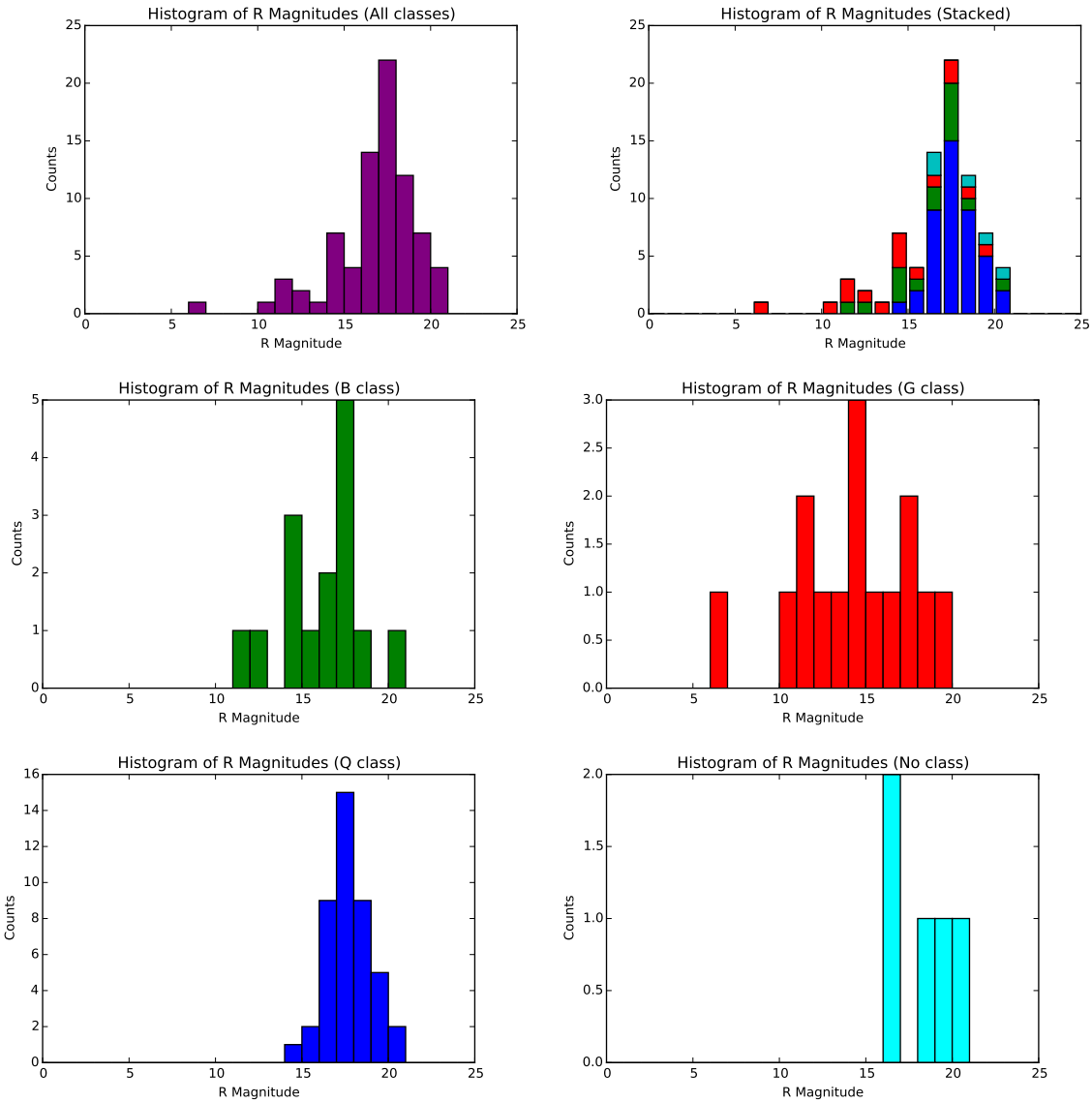

Histograms of apparent magnitudes in the B, V, and R filters, shown with B, G, Q, and U classes.

6.2 Spectral Energy Distributions sorted by class

The green points are from NED, the blue points are from SIMBAD, the purple points are from VizieR, and the red points are at 8.4 GHz from Fermi/LAT.

6.2.1 B Class

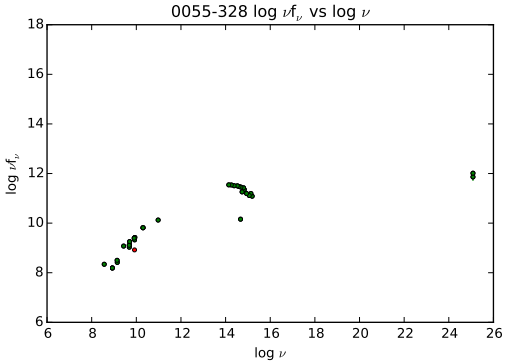
0055-328 log νf_ν vs log ν
log νf_ν
log ν

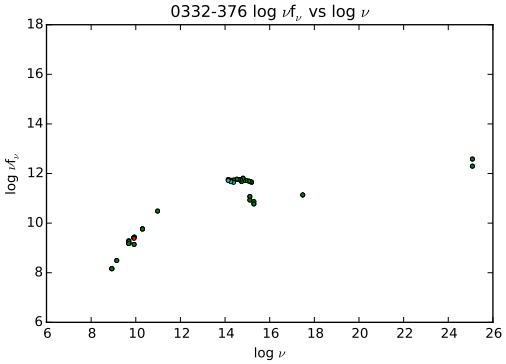
0332-376 log νf_ν vs log ν
log νf_ν
log ν

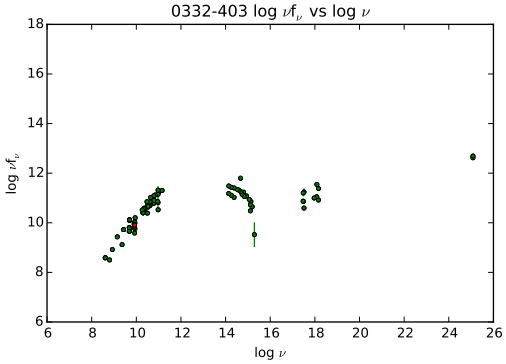
0332-403 log νf_ν vs log ν
log νf_ν
log ν

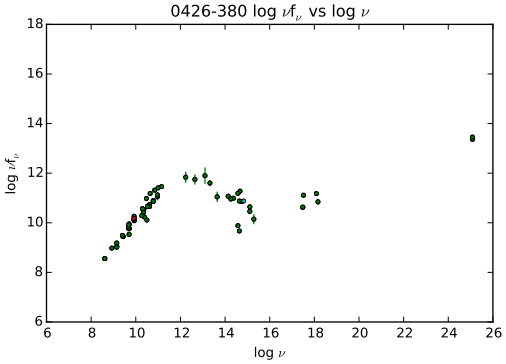
0426-380 log νf_ν vs log ν
log νf_ν
log ν

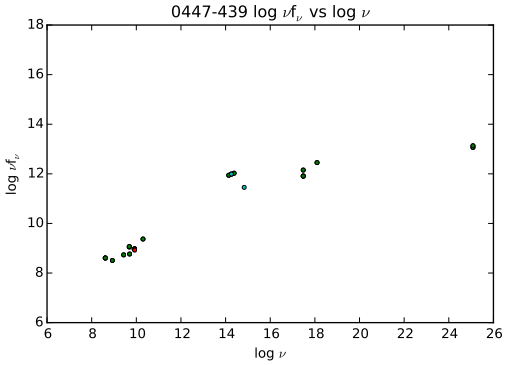
0447-439 log νf_ν vs log ν
log νf_ν
log ν

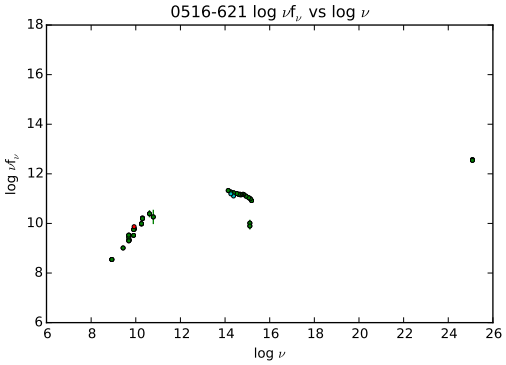
0516-621 log νf_ν vs log ν
log νf_ν
log ν

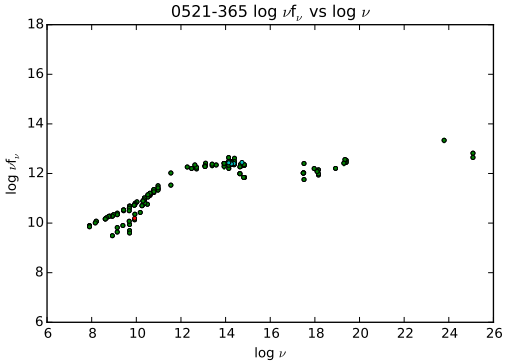
0521-365 log νf_ν vs log ν
log νf_ν
log ν

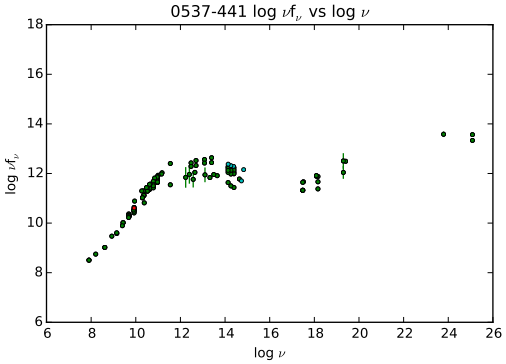
0537-441 log νf_ν vs log ν
log νf_ν
log ν

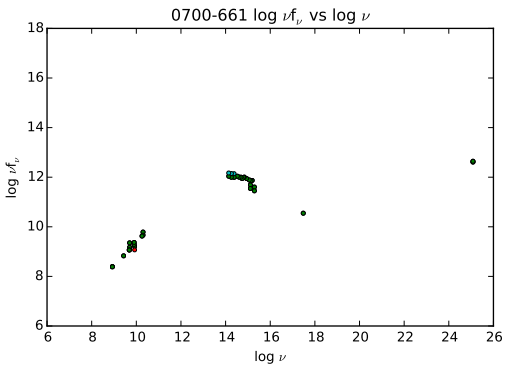
0700-661 log νf_ν vs log ν
log νf_ν
log ν

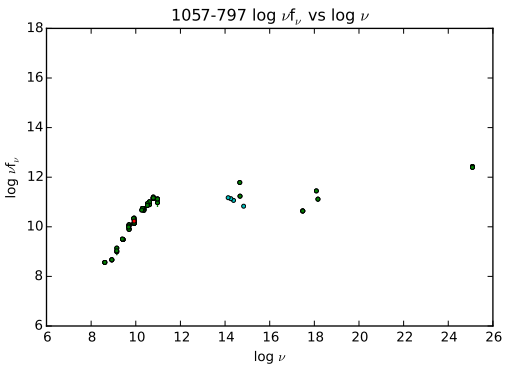
1057-797 log νf_ν vs log ν
log νf_ν
log ν

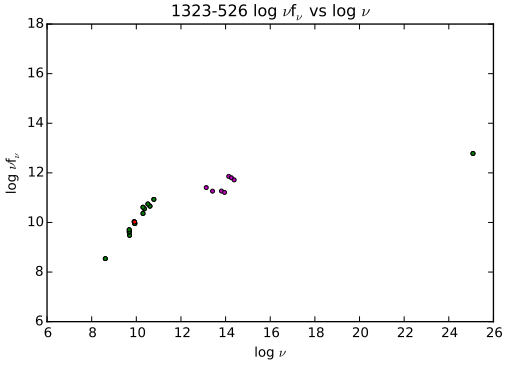
1323-526 log νf_ν vs log ν
log νf_ν
log ν

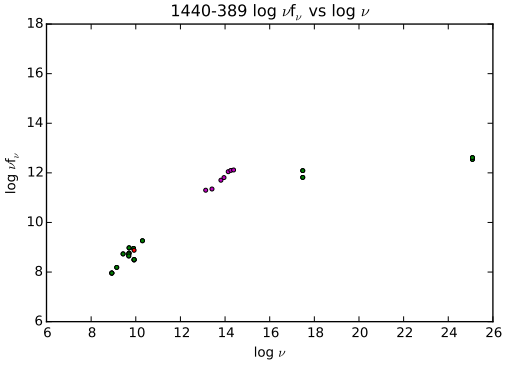
1440-389 log νf_ν vs log ν
log νf_ν
log ν

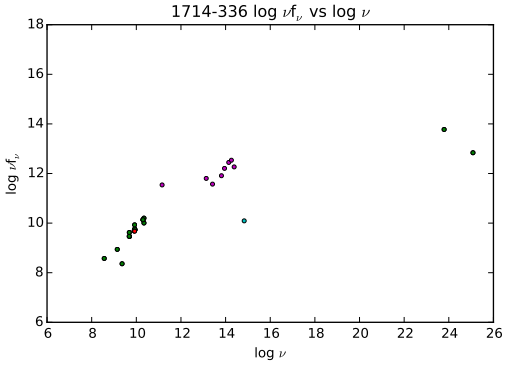
1714-336 log νf_ν vs log ν
log νf_ν
log ν

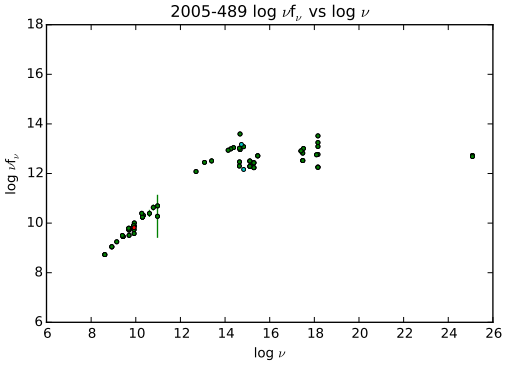
2005-489 log νf_ν vs log ν
log νf_ν
log ν

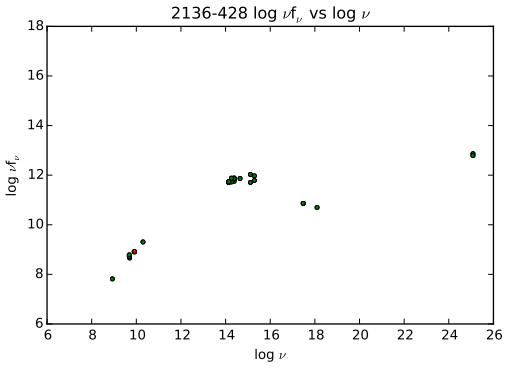
2136-428 log νf_ν vs log ν
log νf_ν
log ν

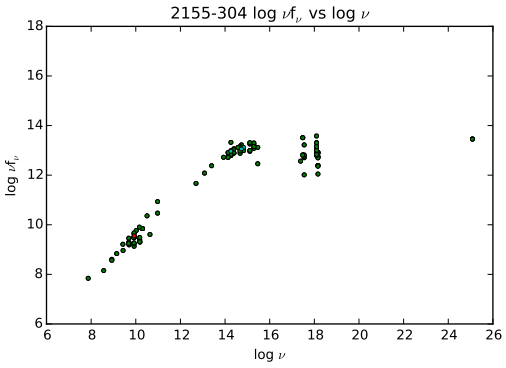
2155-304 log νf_ν vs log ν
log νf_ν
log ν

6.2.2 G Class

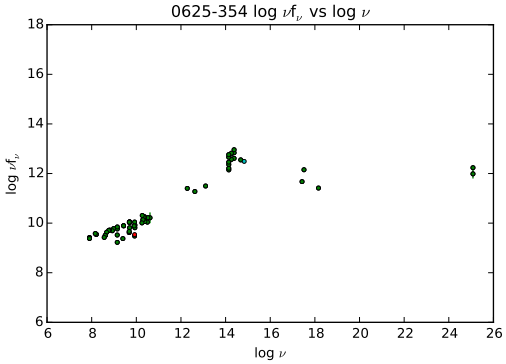
0625-354 log νf_ν vs log ν
log νf_ν
log ν

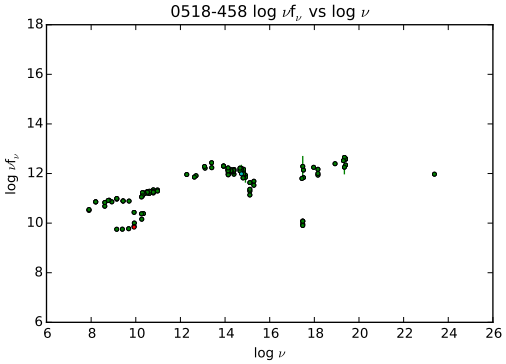
0518-458 log νf_ν vs log ν
log νf_ν
log ν

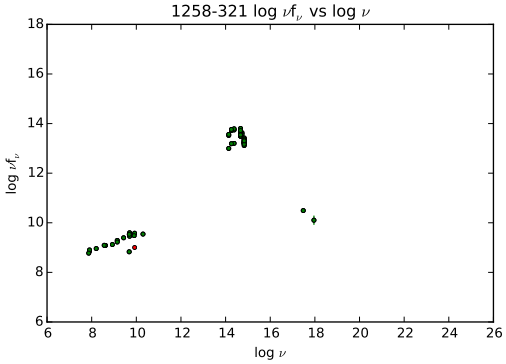
1258-321 log νf_ν vs log ν
log νf_ν
log ν

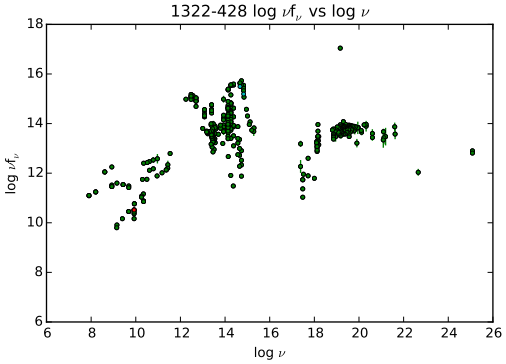
1322-428 log νf_ν vs log ν
log νf_ν
log ν

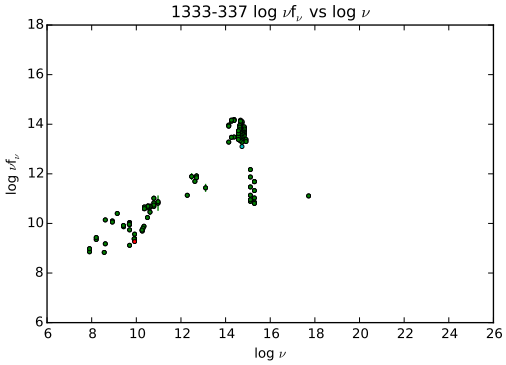
1333-337 log νf_ν vs log ν
log νf_ν
log ν

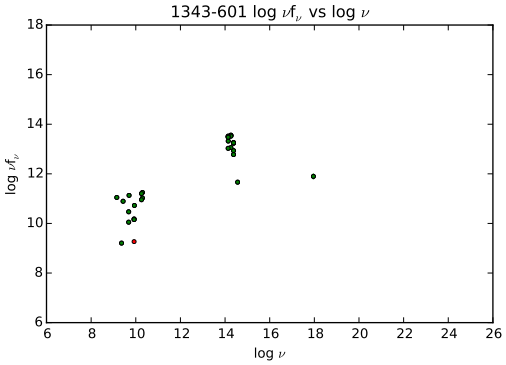
1343-601 log νf_ν vs log ν
log νf_ν
log ν

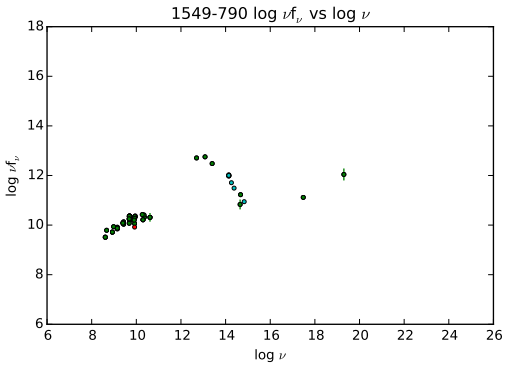
1549-790 log νf_ν vs log ν
log νf_ν
log ν

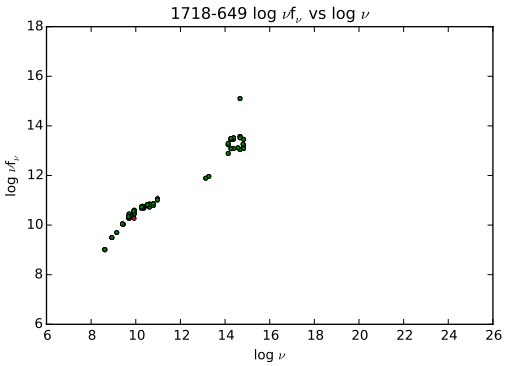
1718-649 log νf_ν vs log ν
log νf_ν
log ν

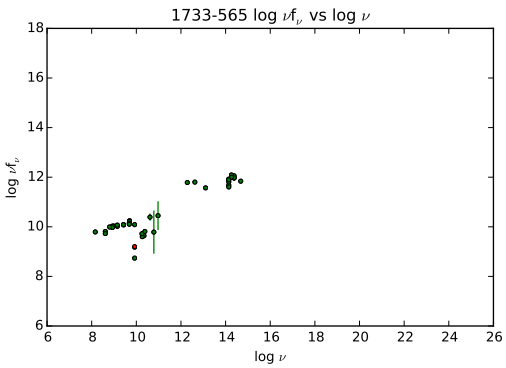
1733-565 log νf_ν vs log ν
log νf_ν
log ν

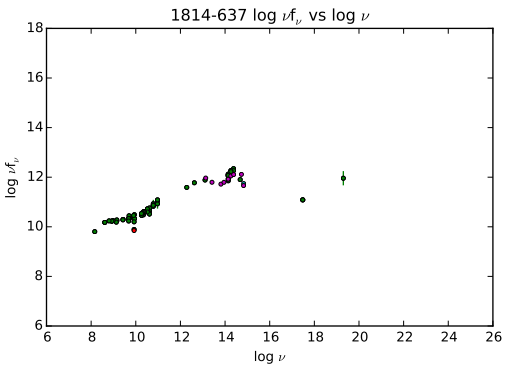
1814-637 log νf_ν vs log ν
log νf_ν
log ν

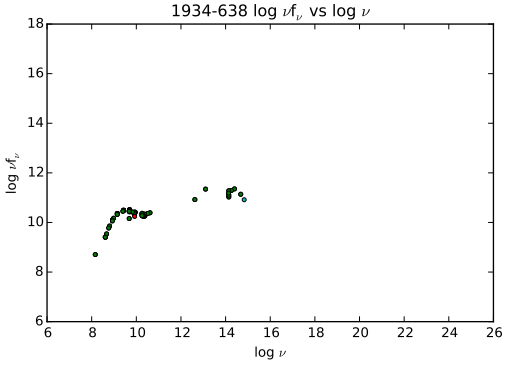
1934-638 log νf_ν vs log ν
log νf_ν
log ν

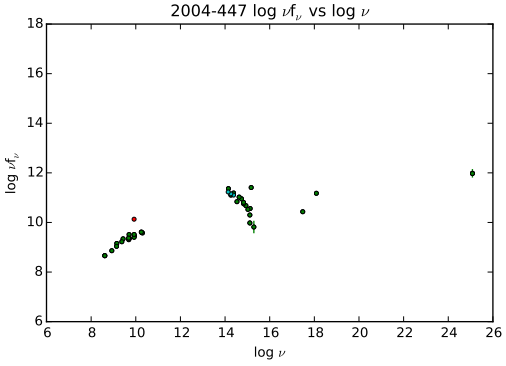
2004-447 log νf_ν vs log ν
log νf_ν
log ν

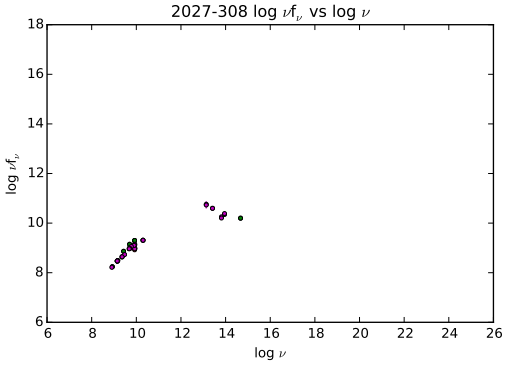
2027-308 log νf_ν vs log ν
log νf_ν
log ν

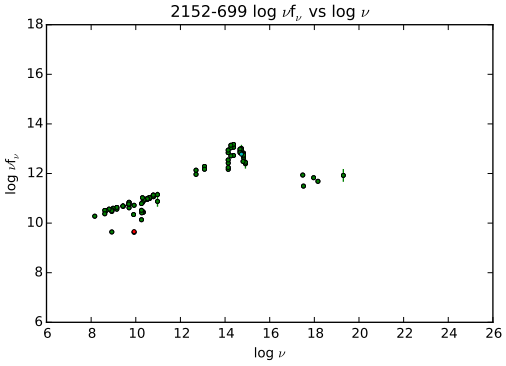
2152-699 log νf_ν vs log ν
log νf_ν
log ν

6.2.3 Q Class

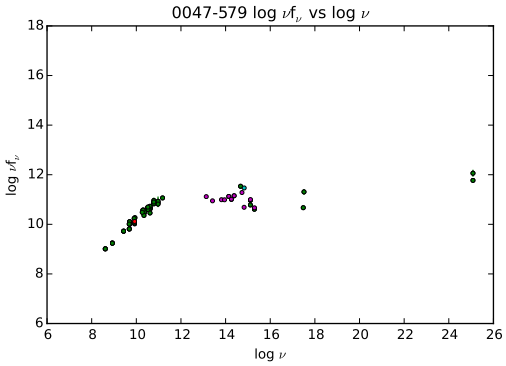
0047-579 log νf_ν vs log ν
log νf_ν
log ν

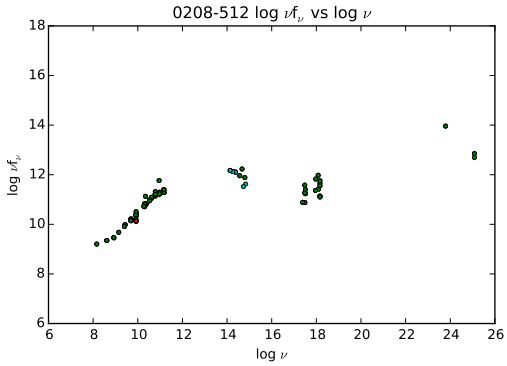
0208-512 log νf_ν vs log ν
log νf_ν
log ν

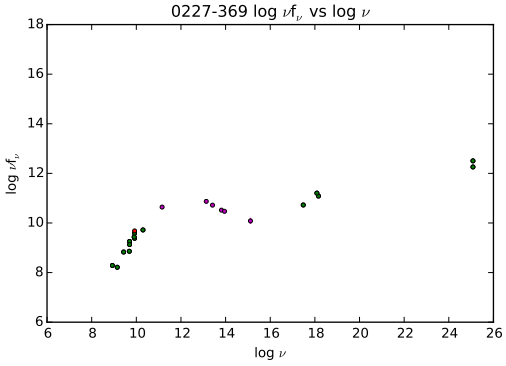
0227-369 log νf_ν vs log ν
log νf_ν
log ν

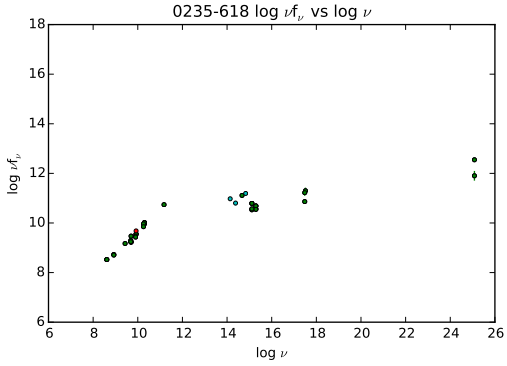
0235-618 log νf_ν vs log ν
log νf_ν
log ν

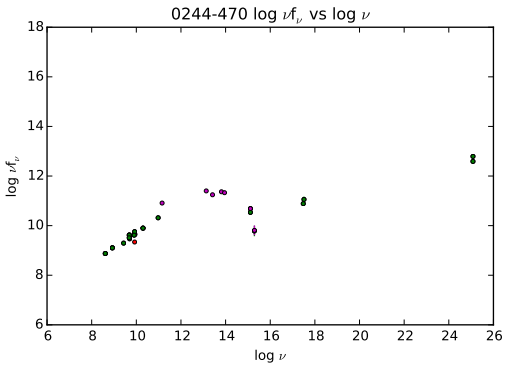
0244-470 log νf_ν vs log ν
log νf_ν
log ν

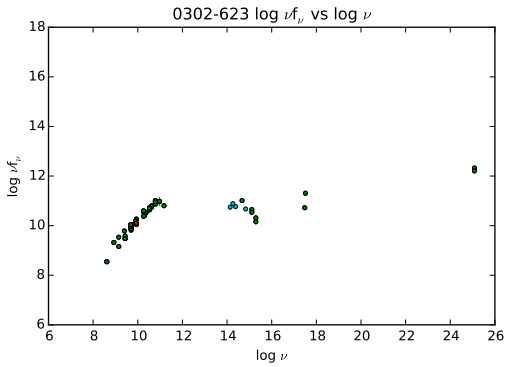
0302-623 log νf_ν vs log ν
log νf_ν
log ν

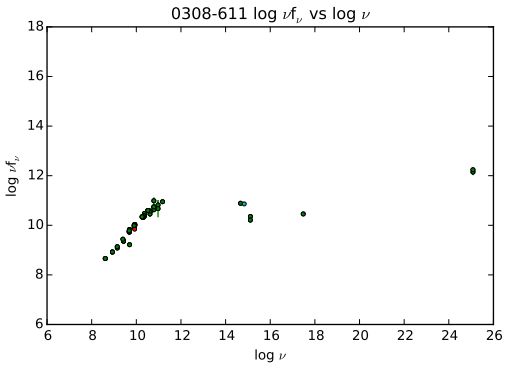
0308-611 log νf_ν vs log ν
log νf_ν
log ν

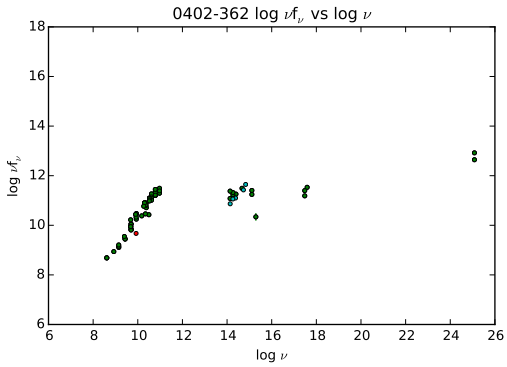
0402-362 log νf_ν vs log ν
log νf_ν
log ν

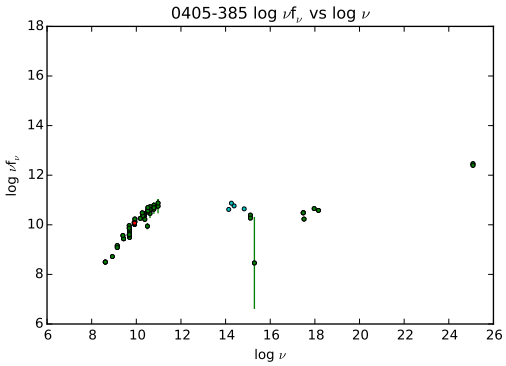
0405-385 log νf_ν vs log ν
log νf_ν
log ν

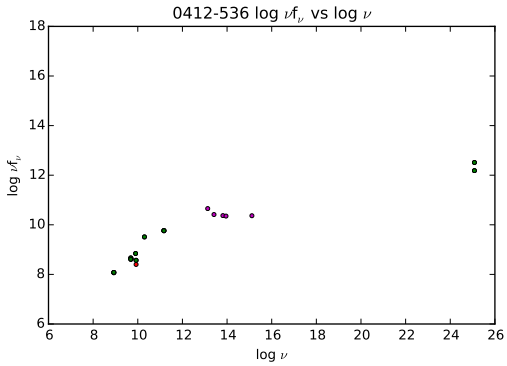
0412-536 log νf_ν vs log ν
log νf_ν
log ν

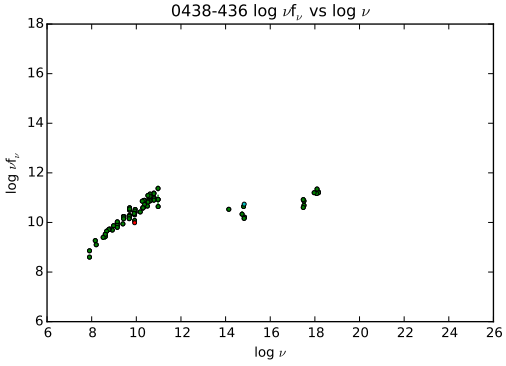
0438-436 log νf_ν vs log ν
log νf_ν
log ν

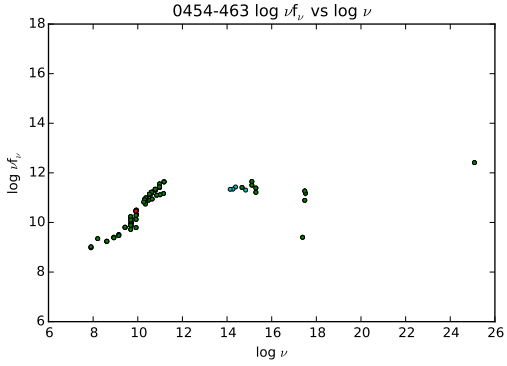
0454-463 log νf_ν vs log ν
log νf_ν
log ν

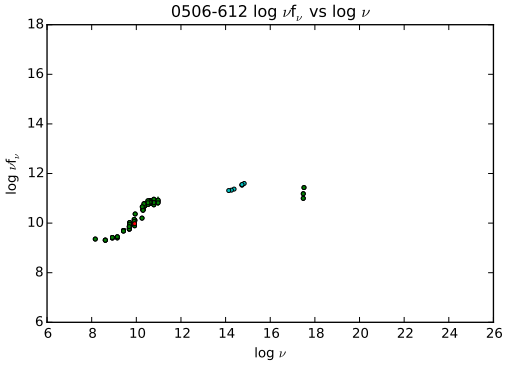
0506-612 log νf_ν vs log ν
log νf_ν
log ν

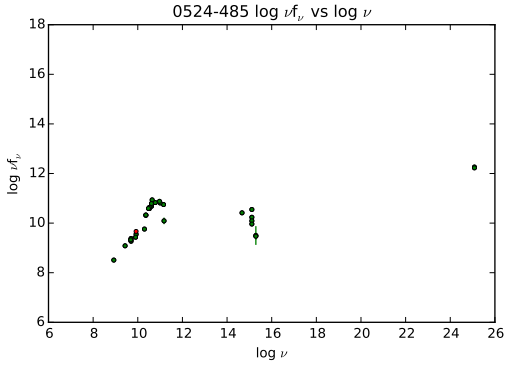
0524-485 log νf_ν vs log ν
log νf_ν
log ν

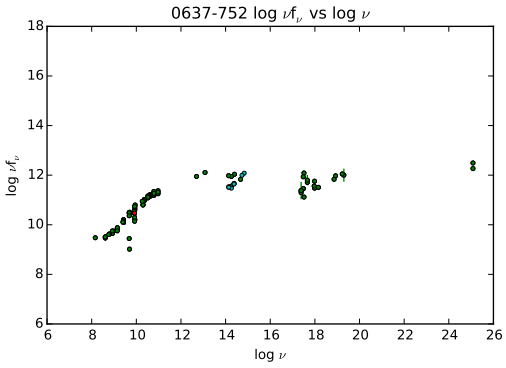
0637-752 log νf_ν vs log ν
log νf_ν
log ν

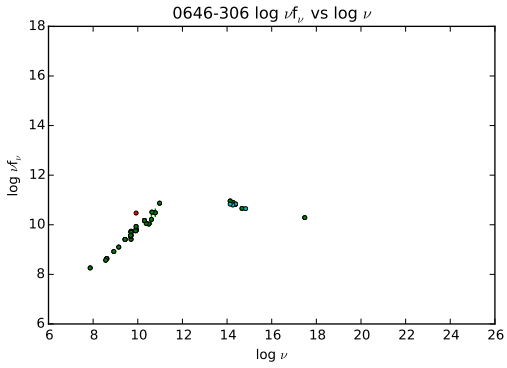
0646-306 log νf_ν vs log ν
log νf_ν
log ν

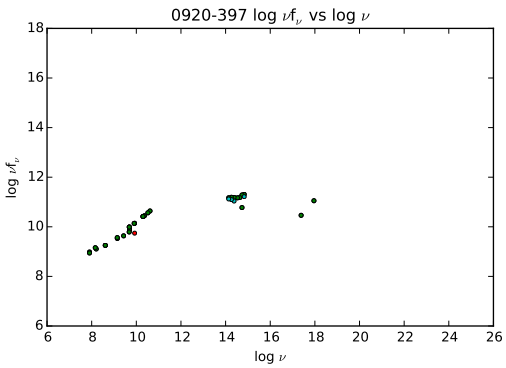
0920-397 log νf_ν vs log ν
log νf_ν
log ν

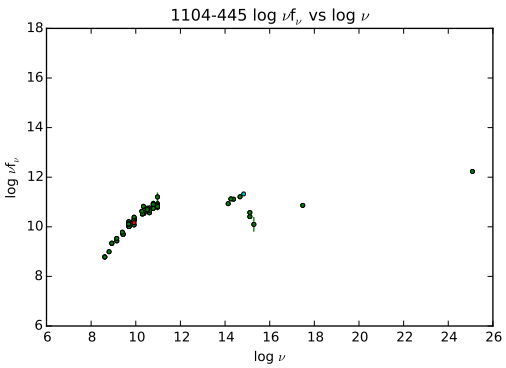
1104-445 log νf_ν vs log ν
log νf_ν
log ν

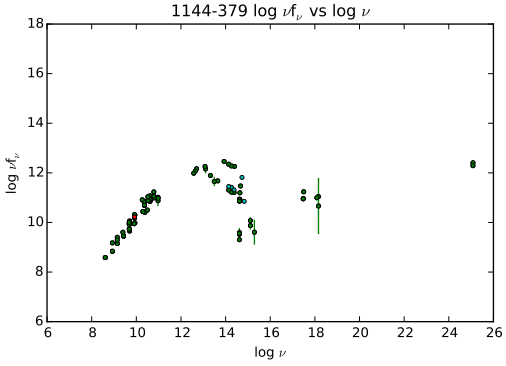
1144-379 log νf_ν vs log ν
log νf_ν
log ν

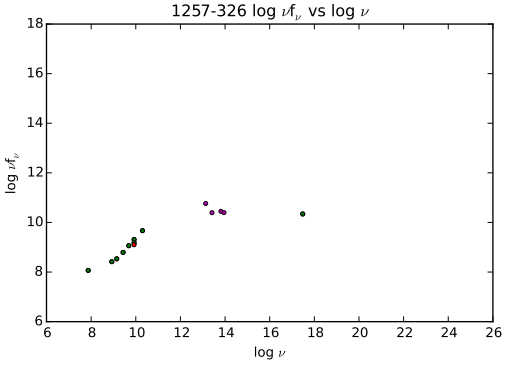
1257-326 log νf_ν vs log ν
log νf_ν
log ν

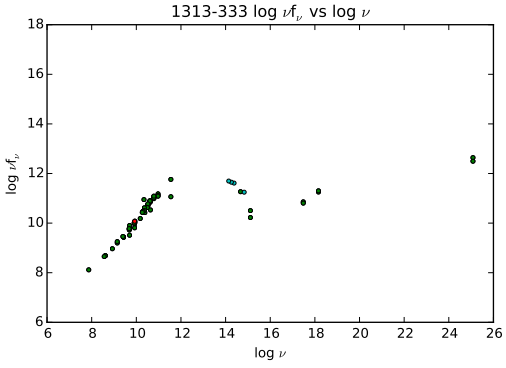
1313-333 log νf_ν vs log ν
log νf_ν
log ν

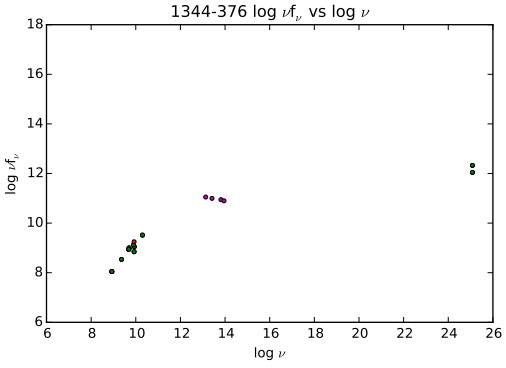
1344-376 log νf_ν vs log ν
log νf_ν
log ν

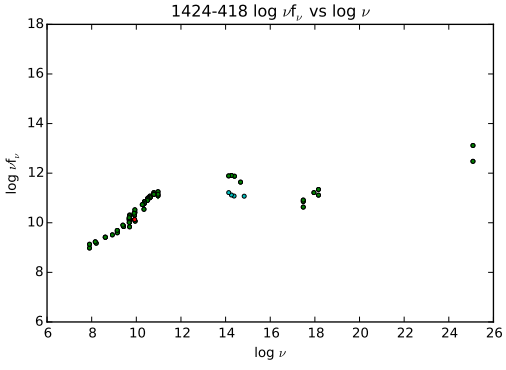
1424-418 log νf_ν vs log ν
log νf_ν
log ν

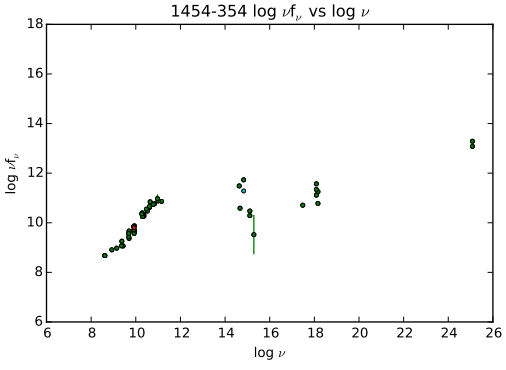
1454-354 log νf_ν vs log ν
log νf_ν
log ν

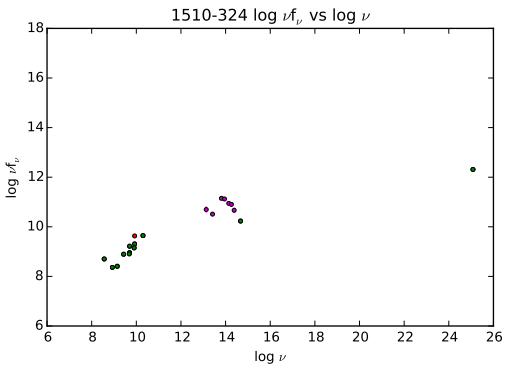
1510-324 log νf_ν vs log ν
log νf_ν
log ν

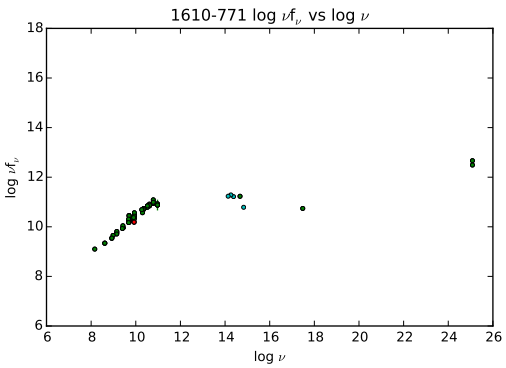
1610-771 log νf_ν vs log ν
log νf_ν
log ν

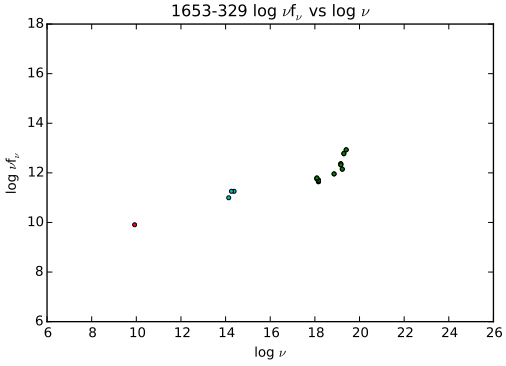
1653-329 log νf_ν vs log ν
log νf_ν
log ν

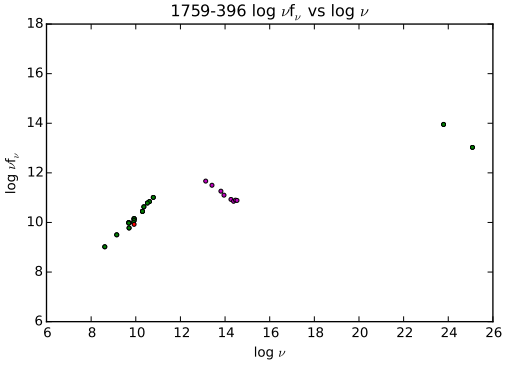
1759-396 log νf_ν vs log ν
log νf_ν
log ν

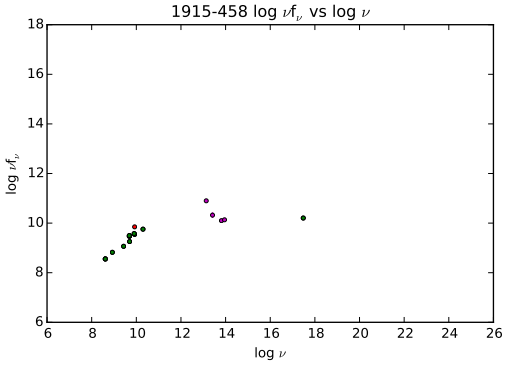
1915-458 log νf_ν vs log ν
log νf_ν
log ν

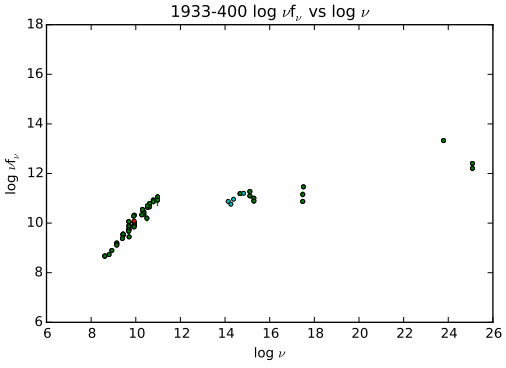
1933-400 log νf_ν vs log ν
log νf_ν
log ν

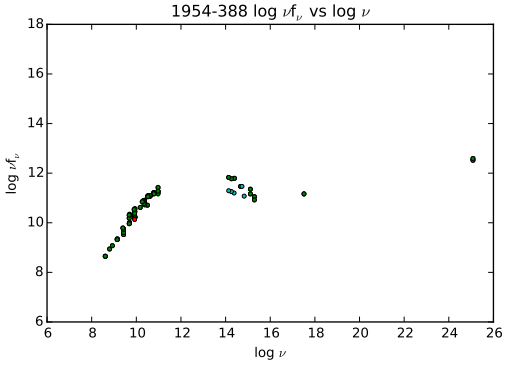
1954-388 log νf_ν vs log ν
log νf_ν
log ν

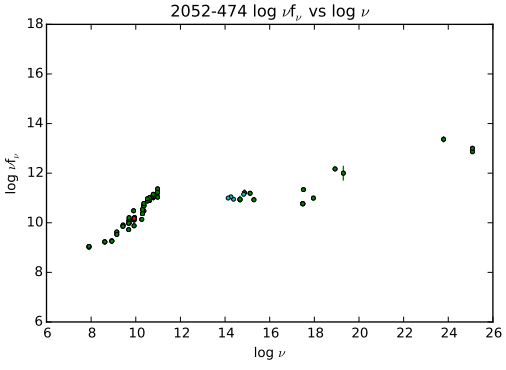
2052-474 log νf_ν vs log ν
log νf_ν
log ν

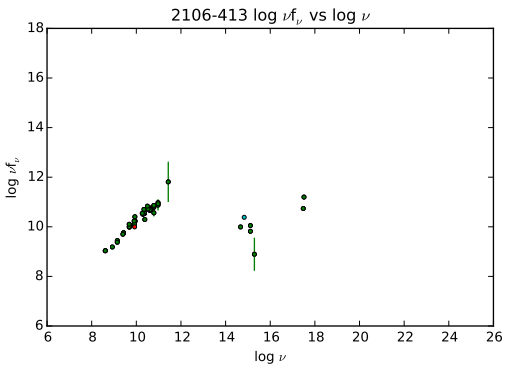
2106-413 log νf_ν vs log ν
log νf_ν
log ν

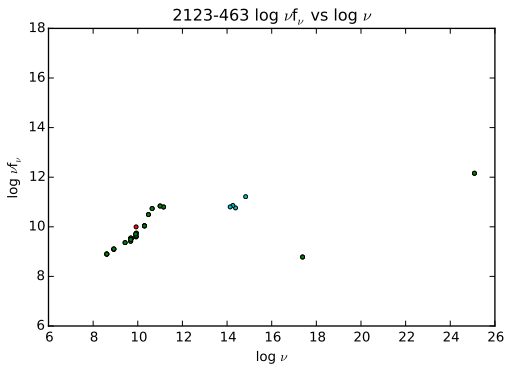
2123-463 log νf_ν vs log ν
log νf_ν
log ν

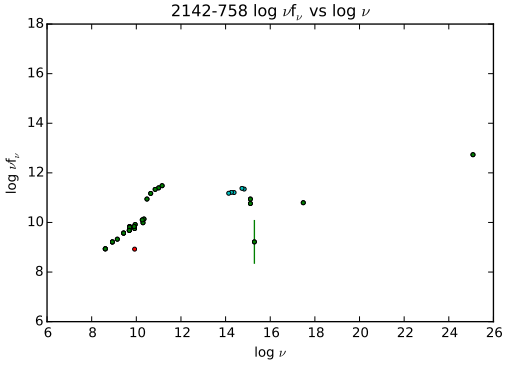
2142-758 log νf_ν vs log ν
log νf_ν
log ν

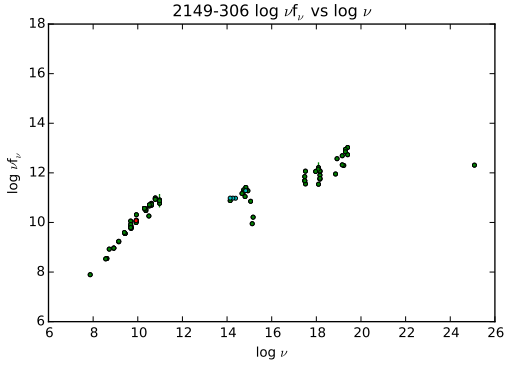
2149-306 log νf_ν vs log ν
log νf_ν
log ν

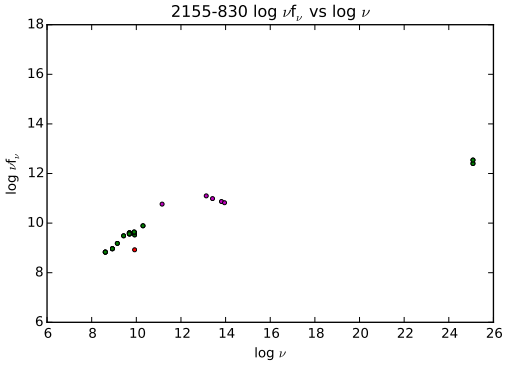
2155-830 log νf_ν vs log ν
log νf_ν
log ν

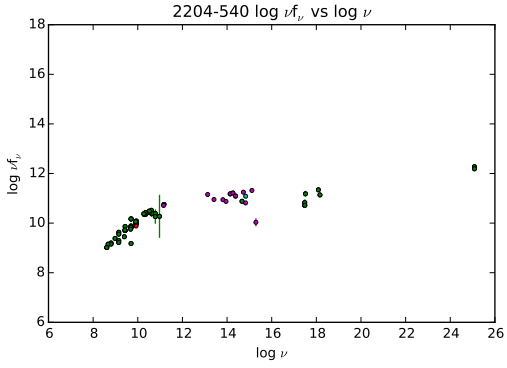
2204-540 log νf_ν vs log ν
log νf_ν
log ν

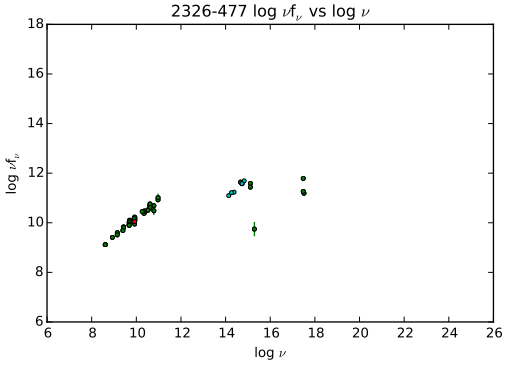
2326-477 log νf_ν vs log ν
log νf_ν
log ν

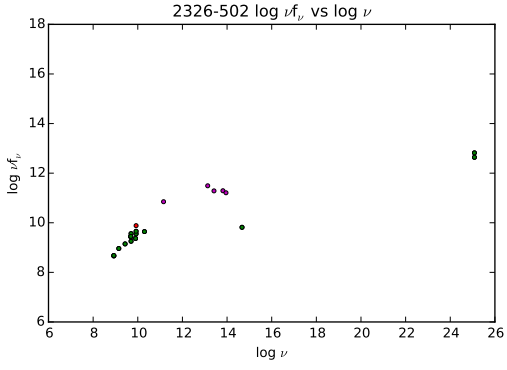
2326-502 log νf_ν vs log ν
log νf_ν
log ν

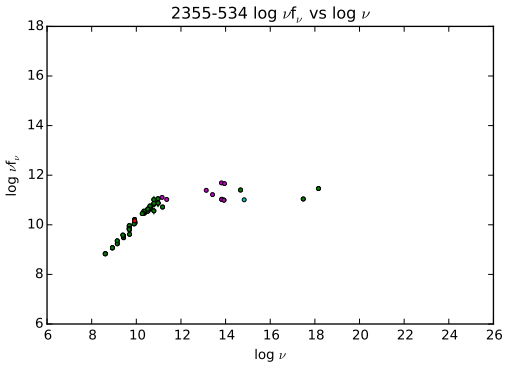
2355-534 log νf_ν vs log ν
log νf_ν
log ν

6.2.4 U Class

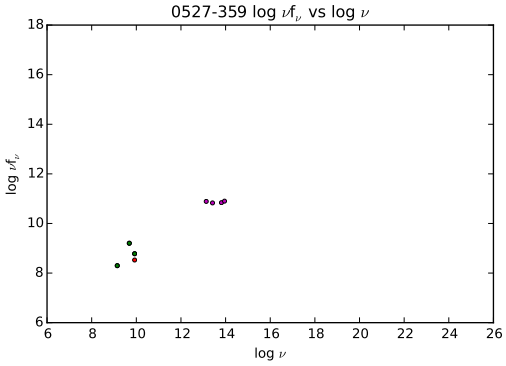
0527-359 log νf_ν vs log ν
log νf_ν
log ν

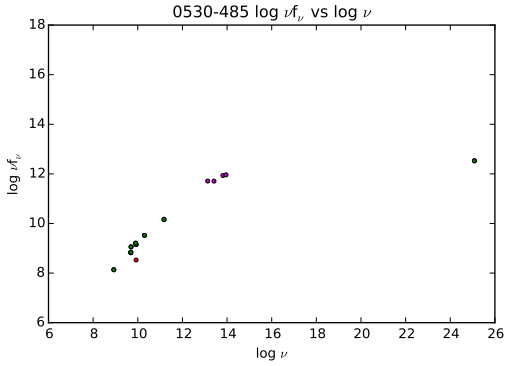
0530-485 log νf_ν vs log ν
log νf_ν
log ν

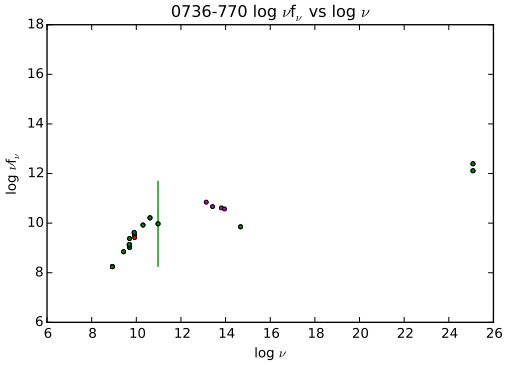
0736-770 log νf_ν vs log ν
log νf_ν
log ν

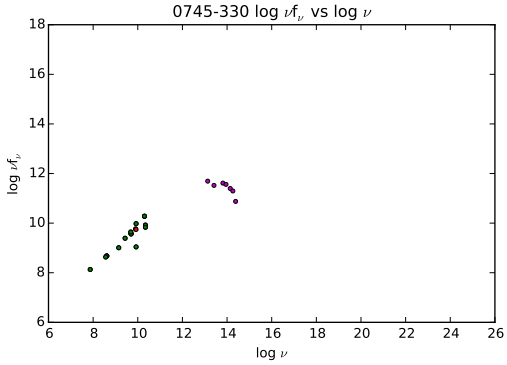
0745-330 log νf_ν vs log ν
log νf_ν
log ν

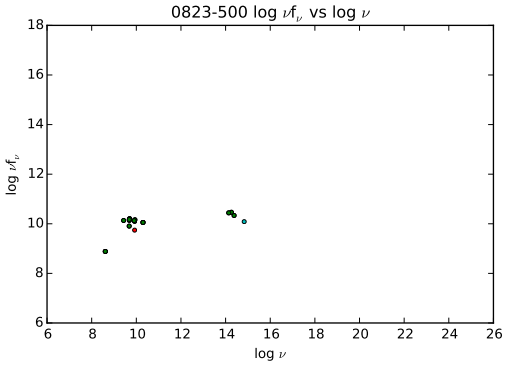
0823-500 log νf_ν vs log ν
log νf_ν
log ν

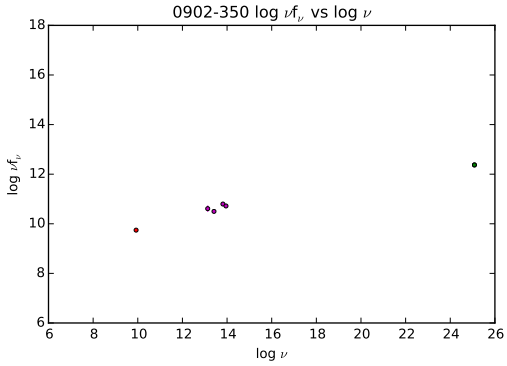
0902-350 log νf_ν vs log ν
log νf_ν
log ν

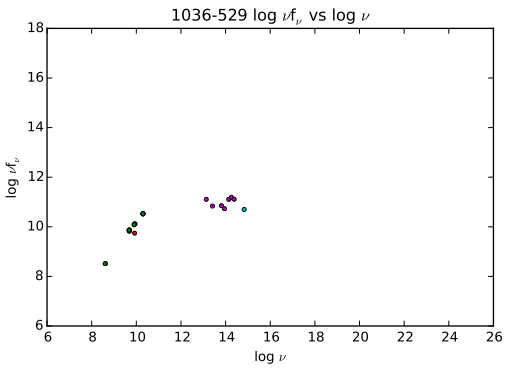
1036-529 log νf_ν vs log ν
log νf_ν
log ν

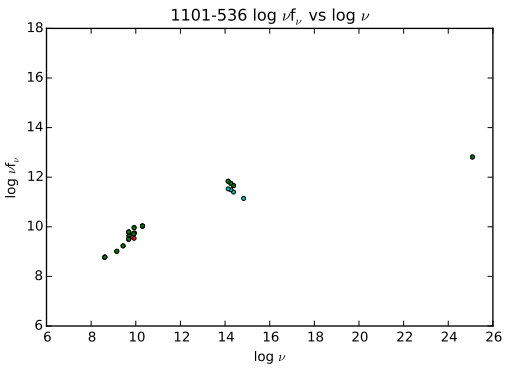
1101-536 log νf_ν vs log ν
log νf_ν
log ν

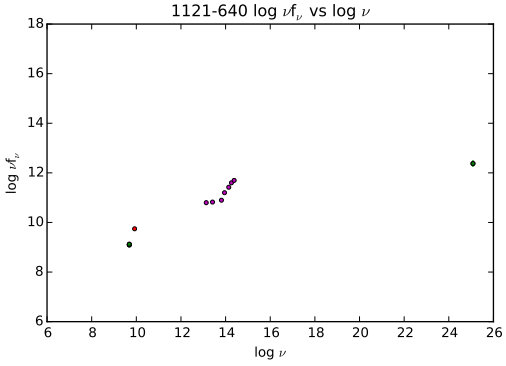
1121-640 log νf_ν vs log ν
log νf_ν
log ν

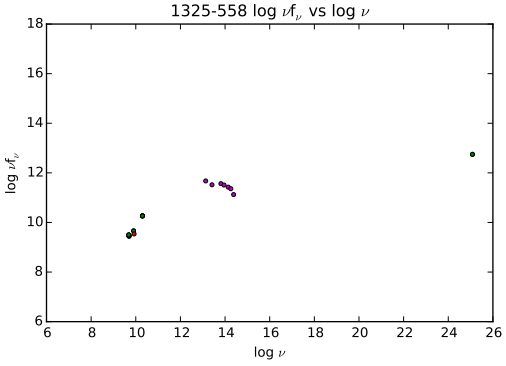
1325-558 log νf_ν vs log ν
log νf_ν
log ν

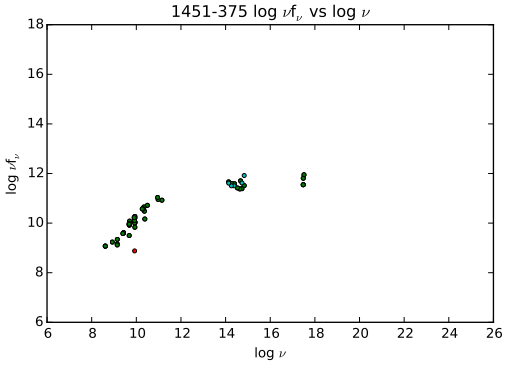
1451-375 log νf_ν vs log ν
log νf_ν
log ν

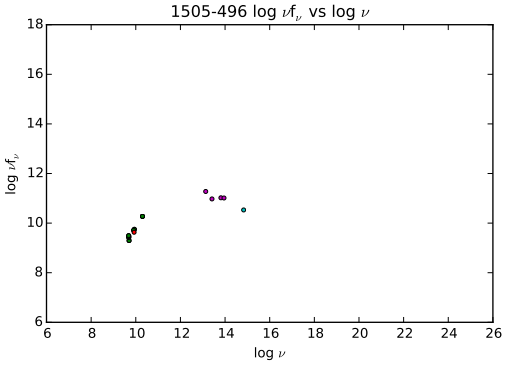
1505-496 log νf_ν vs log ν
log νf_ν
log ν

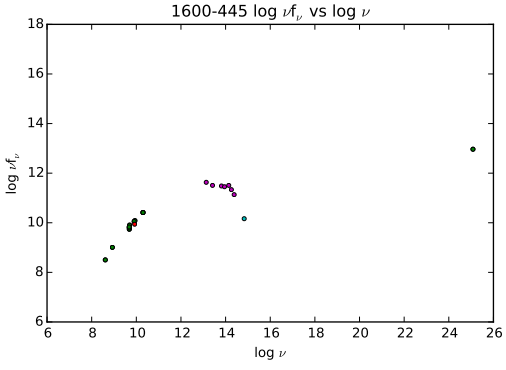
1600-445 log νf_ν vs log ν
log νf_ν
log ν

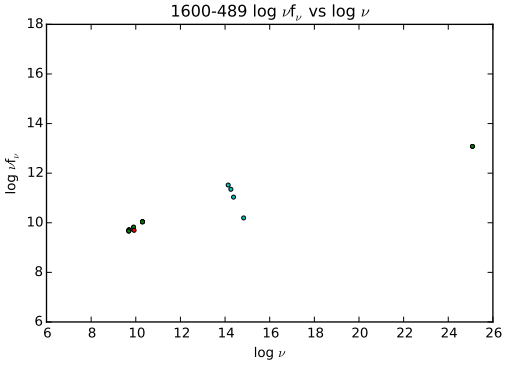
1600-489 log νf_ν vs log ν
log νf_ν
log ν

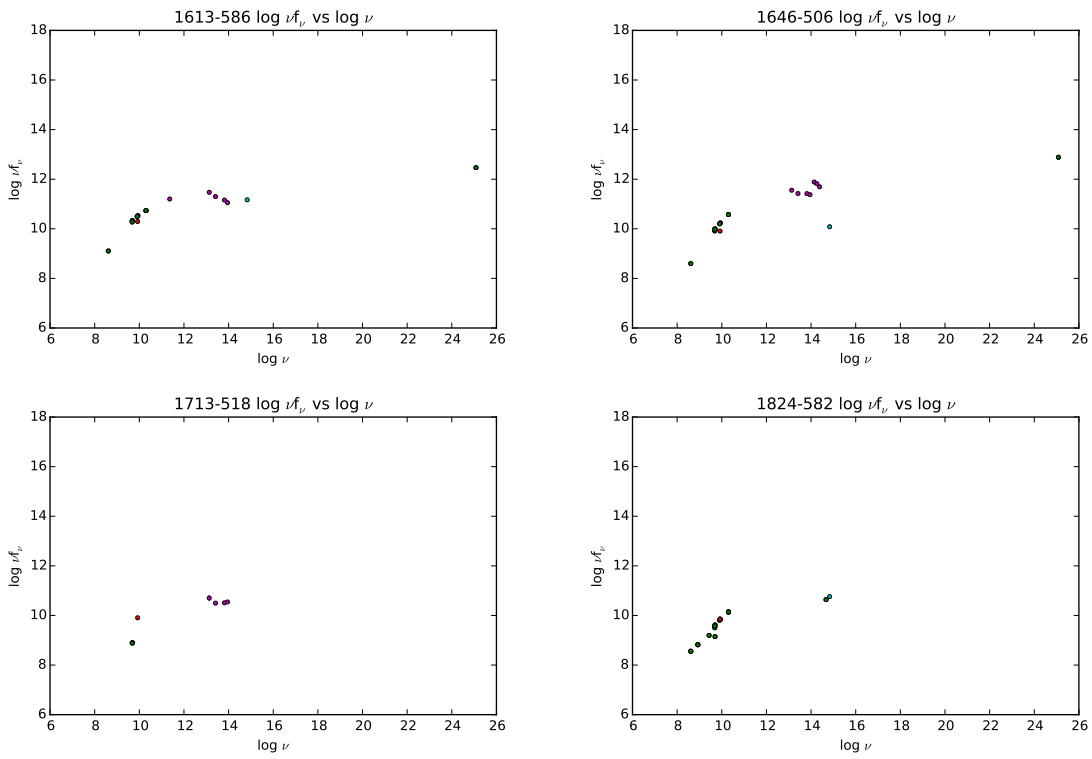

7 Acknowledgements

Research funded with support from the John W. Cox Endowment for the Advanced Studies in Astronomy. This research has made use of the NASA/IPAC Extragalactic Database (NED) which is operated by the Jet Propulsion Laboratory, California Institute of Technology, under contract with the National Aeronautics and Space Administration. This research has made use of the SIMBAD database and the VizieR catalogue access tool, operated at CDS, Strasbourg, France.

Thank you to all of the people who have supported and assisted me in this project. Special thanks goes to Dr. Bev Wills, my wonderful advisor who has helped me immensely in the learning process for this project, as well as with providing direction for my research and edits to the many drafts of this paper. Thank you to Dr. Matthias Kadler and Dr. Dominik Elsaesser, who advised me during my summer in Germany in their research groups, as well as gave me data to work with for the TANAMI sample and ideas for use of MONET. Dr. Cornelia Mueller has also been of great assistance, as she has provided much clarification regarding the TANAMI sample. I would also like to thank my family for helping me through college and supporting me in my endeavours over the past four years, and my entire life thus far.

References

[1] Mueller, C. *High-Resolution Observations of Active Galactic Nuclei in the Southern Hemisphere*. Thesis. Erlangen-Nuernberg, 2014.

[2] Netzer, H. *The Physics and Evolution of Active Galactic Nuclei*, New York, 2013.

[3] Robson, I. *Active Galactic Nuclei*, Chichester, 1996.

[4] Urry, C. M. *Multiwavelength Properties of Blazars, Advances in Space Research*, Vol. 21, Issue 1-2, p. 89, 1998.

[5] Fermi Homepage `http://fermi.gsfc.nasa.gov/science/`

[6] MONET Exposure Time Calculator `http://www.astro.physik.uni-goettingen.de/~hessman/MONET/metc_all.html`

[7] MONET Homepage `https://monet.uni-goettingen.de/`

[8] Starmult Calculator `http://catserver.ing.iac.es/staralt/index.php`

[9] Swift Homepage `http://swift.gsfc.nasa.gov/about_swift/`

[10] TANAMI Homepage `http://pulsar.sternwarte.uni-erlangen.de/tanami/`

[11] The NASA/IPAC Extragalactic Database (NED) is operated by the Jet Propulsion Laboratory, California Institute of Technology, under contract with the National Aeronautics and Space Administration. `http://ned.ipac.caltech.edu/`

[12] 1984ApJ...286..498J

[13] 2000,A&AS,143,9

[14] 2004,MNRAS,350,1195-1209

[15] 2006AJ.131.1163S

[16] 2010A&A.518A.10V

[17] 2010A&A.519A.45O

[18] 2012arXiv1205.2403S

[19] 2013AJ.146.120L

[20] A&AS 143, 23

[21] PNAS.96.9.4749

[22] Bechtold et al 2001

[23] Bechtold et al 2002

[24] Browne et al. 1975

[25] Craig et al, 1997

[26] da Costa et al. 1991

[27] Danziger et al. 1979

[28] Drinkwater et al. 1997

[29] Falomo et al. 1987

[30] Falomo et al. 1993

[31] Fosbury et al 1977

[32] Fosbury et all 1987

[33] Graham. 1978

[34] Healey et al, 2008

[35] Heidt et al 2003

[36] Heidt et al, 2004

[37] Hewitt et al. 1989

[38] Holt et al, 2008

[39] Hook et al 2003

[40] Hunstead et al. 1978

[41] Hunstead+Murdoch 1980

[42] Hunstead et al. 1980

[43] Jackson et al. 2002

[44] Jauncey et al. 1978

[45] Jauncey et al. 1982

[46] Jauncey et al, 1984

[47] Johnston et al, 1995

[48] Jones et al. 2004

[49] Jones et al. 2009

[50] Keel. 1985

[51] Landoni et al, 2013
[52] Landoni et al 2015
[53] Landoni et al 2014
[54] Liang et al, 2003
[55] Lauberts et al. 1989
[56] Mahony et al 2011
[57] Masetti et al 2008
[58] Mathewson et al. 1996
[59] Morton et al. 1978
[60] Oshlack et al 2001
[61] Otrupcek et al. 1991
[62] Perlman et al. 1998
[63] Peterson et al. 1976
[64] Quintana et al. 1995
[65] Sbarufatti et al 2006
[66] Sbarufatti et al. 2009
[67] Stickel et al. 1989
[68] Shaw et al. 2012
[69] Shaw et al, 2013
[70] Smith et al. 2000
[71] So-Em et al 2004
[72] Stickel et al 1988
[73] Stickel et al. 1994
[74] Sulentic et al. 2004
[75] Tadhunter et al, 1993
[76] Tadhunter et al. 2001
[77] Titov et al 2015
[78] Torr et al 2012
[79] Wills et al 1983
[80] Wisotzki et al. 2000
[81] West et al, 1989
[82] White et al. 1988